Particle Image Velocimetry and Infrared Thermography of Turbulent Jet Impingement on an Oscillating Surface

Jewkes, J, Narayanaswamy, R, Lucey, A, Chaugule, V & Narayan, V

Original citation & hyperlink:
Chaugule, V, Narayanaswamy, R, Lucey, A, Narayan, V & Jewkes, J 2018, 'Particle Image Velocimetry and Infrared Thermography of Turbulent Jet Impingement on an Oscillating Surface' Experimental Thermal and Fluid Science, vol. 98, pp. 576-593. https://dx.doi.org/10.1016/j.expthermflusci.2018.06.006

DOI 10.1016/j.expthermflusci.2018.06.006
ISSN 0894-1777

Publisher: Elsevier

Revised version of the manuscript no. ETFS_2018_434
(Initial submission: 17 Apr 2018; Revision requested: 16 May 2018)
Note: The revisions in this manuscript have been highlighted red in colour

Particle Image Velocimetry and Infrared Thermography of Turbulent Jet Impingement on an Oscillating Surface

Vishal Chaugule[1], Ramesh Narayanaswamy[1*], Anthony D Lucey[1], Vinod Narayanan[2] and James Jewkes[3]

[1]Fluid Dynamics Research Group, Department of Mechanical Engineering, Curtin University, Western Australia
[2]Department of Mechanical and Aerospace Engineering, University of California Davis, California, USA
[3]School of Mechanical, Aerospace and Automotive Engineering, Coventry University, Priory St, Coventry, UK
[*]Corresponding author: Ramesh Narayanaswamy r.narayanaswamy@curtin.edu.au +61 8 9266 4483

Abstract

Jet impingement is widely used for forced-convection heat transfer applications and knowledge about its flow structure and heat transfer rate on a static surface are well established. However, the characteristics of jet impingement on an oscillating surface are relatively unknown. This study experimentally investigates the effect of surface oscillation on the fluid dynamics and heat transfer of an unconfined turbulent impinging jet. The Reynolds numbers of the axisymmetric jet are 5000 and 10000, based on the jet-nozzle exit diameter, and the surface is placed at nominal standoff distances of 2 and 5 diameters from the jet-nozzle exit. The surface oscillates in a direction parallel to the jet axis at frequencies of 20 Hz and 50 Hz and at a peak-to-peak displacement amplitude of 0.2 times the jet-nozzle exit diameter. The phase-average and mean flow characteristics at six phases through the surface oscillation cycle, and the steady-state mean heat transfer rate at the oscillating surface, are determined using particle image velocimetry and infrared thermography respectively. These are analyzed and compared with the mean flow and heat transfer characteristics for jet impingement on a static surface. Surface oscillation directly affects the mean axial jet velocities and thence the mean radial velocities, and this effect is greater at locations in the flow-field closer to the surface. This gives rise to lower mean axial and radial strain rates in the impingement region and lower turbulence intensities in the wall-jet region when compared with those for a static surface. The frictional interaction between the impinging jet and oscillating surface induces higher surface temperatures than those on a static surface. These factors reduce the heat transfer rate for jet impingement on an oscillating surface when compared with that on a static surface. The reduction is greater in the impingement region than in the wall-jet region with the stagnation point Nusselt number for an oscillating surface being lower by a maximum value of 15%. Overall, for the range of parameters considered in this study, these findings suggest that surface oscillation in jet impingement weakens the transport phenomena capabilities from those present in the case of a static surface.

Keywords: impinging jet; oscillating surface; particle image velocimetry; infrared thermography

Acknowledgments: The authors gratefully acknowledge support from the Australian Research Council (ARC) through Discovery Project Grant - DP 130103271.

Nomenclature

a_s	peak-to-peak surface oscillation displacement amplitude (mm)
A_f	foil area (mm^2)
A_{fm}	infrared measurement area (mm^2)
B	slot jet nozzle-exit width (mm)
D	axisymmetric jet-nozzle exit diameter (mm)
f_s	surface oscillation frequency (Hz)
h_{conv}	forced-convection heat transfer coefficient = $Q_{fconv}/(T_s - T_{as})$ (W/m^2.K)
H	standoff distance between jet-nozzle exit and surface (mm)
H_m	mean standoff distance between jet-nozzle exit and surface (mm)
I_f	current supplied to the foil (A)
k	thermal conductivity of air = 0.02514 (W/m.K)
k_f	thermal conductivity of Inconel-600 alloy = 14.8 (W/m.K)
N	number of oscillation cycles
P_{fm}	perimeter of infrared measurement region (mm)
Q_{cond}	conduction heat flux (W/m^2)
Q_f	input heat flux (W/m^2)
Q_{fconv}	forced-convection heat flux (W/m^2)
Q_{nconv}	natural-convection heat flux (W/m^2)
Q_{rad}	radiation heat flux (W/m^2)
s_f	foil thickness (μm)
t	time (s)
t_l	integral flow time-scale = D/U_0 (s)
$\overleftrightarrow{T}$	total time of velocity sampling (s)
T_{am}	ambient fluid temperature (K)
T_{as}	local adiabatic surface temperature (K)
T_j	jet temperature at jet-nozzle exit (K)
T_s	local heated surface temperature (K)
$\overleftrightarrow{T}_s$	surface oscillation period (s)
u, v	instantaneous axial and radial velocities (m/s)
U, V	mean axial and radial velocities (m/s)
$\tilde{u}$, $\tilde{v}$	phase-correlated axial and radial velocities (m/s)
u', v'	axial and radial turbulence velocity fluctuations (m/s)
$\langle u \rangle$,$\langle v \rangle$	phase-average axial and radial velocities (m/s)
$\overline{u'v'}$	Reynolds stress (m/s)^2
U_0	jet bulk-flow speed (m/s)
u_{rms}, v_{rms}	

v_s	root-mean-square axial and radial turbulence velocity fluctuations (m/s)
V_f	peak surface oscillation velocity (m/s)
X, Y, Z	electrical potential difference across the foil (Volts)
	spatial coordinates (m)
Bi	Non-dimensional quantities
Gr	Biot number = $h_{conv}s_f/k_f$
Nu	
Pr	Grashof number, based on a length scale A_{fm}/P_{fm}, = $\frac{\left(A_{fm}/P_{fm}\right)^3 g\beta(T_s - T_{am})}{\nu^2}$
Ra	Nusselt number = $h_{conv}D/k$
Re	Prandtl number of air = 0.71
St_s	Rayleigh number = *GrPr*
	Reynolds number = $\rho U_0 D/\mu$
	Surface oscillation Strouhal number = $f_s a_s/U_0$
β	
ε	Greek symbols
μ	volumetric thermal expansion coefficient of air = $1/T_{am}$ (K^{-1})
ν	emissivity of black-paint coated foil = 0.88
ρ	dynamic viscosity of air = 1.82×10^{-5} (kg/m-s)
σ	kinematic viscosity of air = 15.1×10^{-5} (m^2/s)
□	density of air = 1.2047 (kg/m^3)
	Stefan-Boltzmann constant = 5.67×10^{-8} (W/m^2K^4)
	surface oscillation phase (displacement position)

1. Introduction

Jet impingement has been a subject of significant research because of its widespread use in forced-convection heat transfer applications involving heating, drying and cooling. Although simple in its configuration, an axisymmetric jet impinging on a flat surface involves complex non-linear thermo-fluid interactions occurring not only in the impingement region of streamline curvature but also in the wall-jet region of parallel flow along the surface. Thermo-fluid dynamics of impinging jets have been extensively studied to understand these interactions and to determine pertinent parameters and factors that govern them (Gauntner et al. 1970; Martin 1977; Hrycak 1981; Jambunathan et al. 1992; Viskanta 1993; Zuckerman and Lior 2006; and, Carlomagno and Ianiro 2014). The jet Reynolds number Re, based on the exit diameter D of an axisymmetric jet-nozzle and the jet bulk-flow speed U_0, and the standoff-distance H between the jet-nozzle exit and the surface (usually non-dimensionalised as H/D) are critical for jet impingement. However, other factors such as jet-nozzle geometry, radial distance from the stagnation point, spatial confinement around the jet, and the geometrical profile of the impingement surface also affect thermo-fluid characteristics in jet impingement.

Previous studies have investigated jet impingement based on various parameters and different factors, not only to examine their effect on jet flow-field and heat transfer but also to improve the transport phenomena capabilities of the jet. A few of these included a pulsating jet (Medina et al. 2013), a modified jet-nozzle geometry (Violato et al. 2012), a confined jet (Choo and Kim 2010) and a swirling jet (Ahmed et al. 2017). Apart from altering jet features, some studies incorporated modified geometry and dynamics of the impingement surface by using a curved surface (Tawfek 2002), a flat surface with dimples (Kanokjaruvijit and Martinez-botas 2005), a rotating surface (Astarita and Cardone 2008), a horizontally moving surface (Mobtil et al. 2014), and an oscillating surface (Nasif et al. 2015b).

In regards to axisymmetric jet impingement on a dynamic surface, the surface motion can be categorized into two directions, namely, motion in a direction that is perpendicular to the jet axis, and that which is parallel to the jet axis. Examples of the first type are a surface moving with a horizontal velocity, such as a conveyor belt (Senter and Solliec 2007), and a surface rotating about the jet axis, such as a rotor-stator system in a gas turbine (Nguyen et al. 2012). By contrast, the purpose of the present paper is to study the effect of the second type of surface motion, where a surface undergoes forced oscillation, in a direction parallel to the jet axis. Jet

impingement on such a surface finds application in areas such as engine piston cooling and jet impingement cooling using piezo-electric vibrating components.

Only a few studies of jet impingement on an oscillating surface have been reported in literature. One of the earliest was by Yang et al. (1999) who experimentally studied heat transfer of a confined jet impinging on a reciprocating concave target surface for application in engine piston cooling. The H/D value was fixed at 22.5, while the jet Re varied between 17500 and 43200 for surface reciprocating frequencies f_s between 0.833 Hz to 2.08 Hz. The instantaneous Nusselt number Nu at a given spatial location on the surface was found to be considerably different from the phase-averaged Nu at the same location due to unsteadiness of the reciprocation. The maximum heat transfer was clearly determined to be at the stagnation point for both reciprocating and non-reciprocating concave surfaces, with an enhancement at this location observed for Re = 40000 and f_s = 2.08 Hz, which was 3.2 times that of the non-reciprocating case. They concluded that the reciprocating action of the surface contributed to the increase of spatially averaged Nu.

The heat transfer of a confined circular jet impinging upon a reciprocating surface with ribs was investigated by Chang et al. (2000), for parameters in the range of $10000 < Re < 25000$ and $0.83 \text{ Hz} < f_s < 1.67 \text{ Hz}$. They observed a 20% reduction in the convection heat transfer coefficient at the smallest surface reciprocation frequency and 240% improvement at the largest frequency, compared with that for a confined static surface. Wen (2005) was the first to investigate flow structures and heat transfer in swirling jet impingement on a heated vibrating surface. The study was carried out for Re between 440 and 27000 and H/D between 3 and 16, with sinusoidal surface oscillation at frequencies and displacement amplitudes in the range of $0.3 \text{ Hz} < f_s < 10.19 \text{ Hz}$ and $0.5 \text{ mm} < a_s < 8.1 \text{ mm}$ respectively. The heat transfer investigations, and the presented correlations, showed that Nu was strongly dependent on surface vibrational parameters and Re, and that the heat transfer coefficient increased with increasing frequency and displacement amplitude.

Ichimiya and Yoshida (2009) studied the effect of a confined slot jet of width B impinging on a heated oscillating surface, and provided measurements of turbulence intensities in the flow-field and the heat transfer coefficients. The experimental parameters for this study varied over Re between 1000 and 10000, H/B between 1 to 4, f_s up to 100 Hz, and a_s of 0.5 mm and 1 mm. They showed that the jet area from the nozzle exit expanded further outwards from that observed for a static surface and that the turbulence intensity increased with increasing

frequency at H/B = 1. The heat transfer estimation for small H/B and low Re and f_s showed enhancement from that for a static surface. However, for large H/B and higher Re and f_s values the heat transfer rate was reduced.

Klein and Hetsroni (2012) examined heat transfer from a heated vibrating silicon chip placed under a confined impinging micro-slot jet in the range of 756 < Re < 1260. The slot width was 220 μm and the silicon chip was vibrated at frequencies up to f_s = 400 Hz and at micro-amplitudes of up to a_s = 150 μm using a piezoelectric actuator. A maximum increase of 34% in the heat transfer coefficients was measured for the case of Re = 1260 at f_s = 246 Hz at the highest displacement amplitude. They attributed this increase to the renewal of boundary layer caused by the vortices created by surface vibration.

Nasif et al. (2015a) reported a numerical investigation of the transient thermal effects in a circular jet impinging on a reciprocating surface using a volume-of-fluid (VOF) method. The jet Re was 3000 and f_s values were 33 Hz and 100 Hz. They concluded that surface cooling was more effective at lower velocities of surface during its oscillation cycle, and that the maximum heat transfer occurred in the impingement region. They also found the occurrence of the maximum Nu at the stagnation point lagged that of the maximum relative velocity between the jet and surface by a short time.

In all of the aforementioned studies the emphasis was on the effect of surface oscillation on local and average heat transfer coefficients, rather than on the impinging jet flow-field. Although Ichimiya and Yoshida (2009) reported measurements of turbulence intensities, the fluid dynamics of jet interaction with surface oscillation was not examined in detail. The findings from existing published literature show that jet impingement heat transfer is enhanced as well as diminished by surface oscillation when compared with that for a static surface, but there is insufficient data to clearly understand and establish the relationship between modification of heat transfer and impinging-jet flow features due to surface oscillation.

Furthermore, it is known that mean-flow properties and turbulence characteristics of impinging jet are important in the heat removal process (Gardon and Akfirat 1965; Carlomagno and Ianiro 2014), and it is expected that these will change due to the effect of surface oscillation. Therefore, the emphasis of the present study is to investigate the fluid-dynamics characteristics of jet impingement on an oscillating surface, and determine their effect on the resulting heat transfer characteristics, so as to fundamentally establish the relation between heat transfer modification and the flow features. Accordingly, the physical system considered in

the present study consist of (i) jet impingement on a heated static surface, and (ii) jet impingement on a heated oscillating surface. The former serves as a control against which to evaluate the effects of surface oscillation in the jet impingement system.

The impinging-jet configuration in the present work consists of a single, submerged and unconfined axisymmetric jet, at Reynolds numbers Re = 5000 and 10000, impinging perpendicularly onto flat static and oscillating surfaces. The nominal mean standoff distances for the static and oscillating surfaces are H_m/D = 2 and 5, where the surface undergoes oscillation at frequencies f_s = 20 Hz and 50 Hz at a peak-to-peak displacement amplitude a_s = 2.5 mm. Time-resolved two-dimensional two-component (2D-2C) particle image velocimetry (PIV) is used to obtain instantaneous velocity components at various phases (displacement positions) of surface oscillation in jet impingement on an oscillating surface. Triple decomposition of these velocities is performed to determine the mean and phase-average velocity components, the root-mean-square velocity fluctuation components, and the Reynolds stress. Infrared thermography (IRT) is used to obtain steady-state mean temperatures of the oscillating surface. The IRT measurements are obtained independently of the PIV measurements and are used to determine the convection heat transfer coefficients at the surface. The above mentioned mean-flow and heat transfer quantities are compared and analyzed with those of jet impingement on a static surface placed at the corresponding mean standoff distances. This is done in order to ascertain the effect an oscillating surface has on an impinging-jet flow, and thereby on the convection heat transfer rate.

2. Methods

2.1 Experimental system

The experiments on jet impingement on an oscillating surface were carried out in the Thermo-Fluids Research Laboratory at Curtin University. A schematic of the experimental set-up developed and used for this study is shown in Fig. 1. Two branches of air flow, one clean and the other seeded with tracer particles, are used for PIV experiments, while only the clean air flow is used for IRT experiments. Both these flows are metered and then merged in a Y-hydraulic fitting before entering into a straight circular jet pipe. A flow straightener is installed in the entrance of the pipe to eliminate any swirl generated by the Y-hydraulic fitting. The circular jet pipe is made up of three parts: at the flow entrance is a 400 mm long polyvinyl chloride (PVC) pipe with an inner diameter of 23.4 mm; this section is followed by a 100 mm

long PVC pipe of 17.6 mm inner diameter; and it is attached to a copper reducer coupling that forms the jet nozzle.

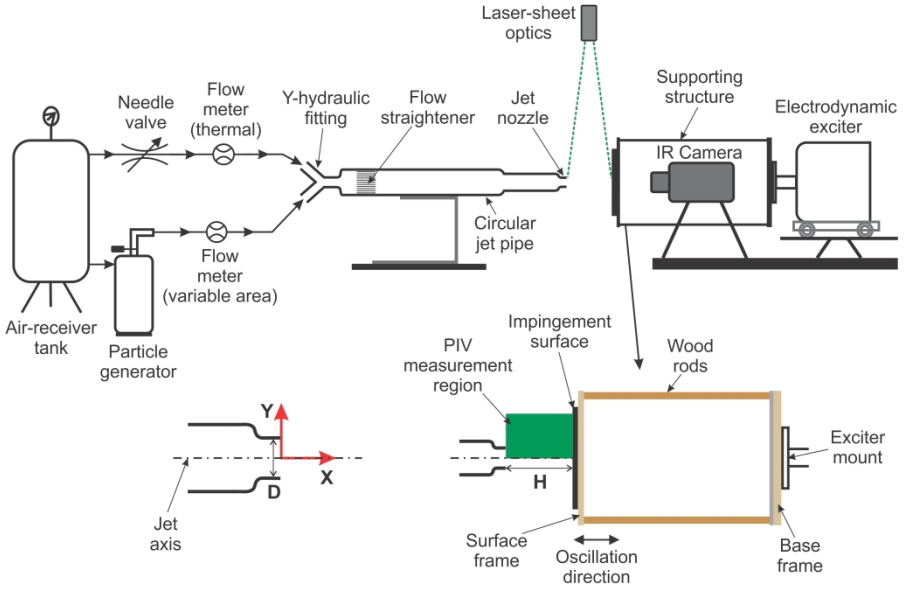

Fig. 1 Schematic of the experimental system

The jet nozzle has a 1.5 mm thick wall and an exit plane inner diameter of 12.6 mm that forms the jet exit diameter D. It has a straight section of length $0.87D$ downstream of the location where the contraction of the nozzle ends. The total length of the jet pipe ensures adequate mixing of the clean air flow and the seeded flow so that the jet exits with uniform seeding. The X and Y axes illustrated in Fig. 1 represent the axial and radial flow directions respectively. A Perspex square box (not shown in Fig. 1) of side 300 mm is placed around the jet-nozzle exit to increase the ambient tracer-particle seeding density; the dimensions of the box are large enough to ensure that the impinging jet is unconfined.

The impingement target is an Inconel-600 alloy foil of area A_f = 156 × 156 mm^2 and thickness s_f = 25 μm. The electrical resistivity of the alloy is 103 × 10^{-8} Ohm.m and its thermal conductivity is k_f = 14.8 W/m.K. The spatial temperature distribution of the foil on its non-impingement surface was measured using an infrared camera. In order to provide this measurement surface of the foil at a 90° incidence angle to the infrared camera and to simultaneously have the provision of a heated oscillating impingement surface a suitable supporting structure was fabricated. This structure enables the attachment of the impingement surface to an electrodynamic exciter, with the infrared camera placed stationary within the

structure as shown in Fig. 1. The infrared camera is mounted independently and in isolation from both the vibration exciter and the supporting structure. An enlarged view of the supporting structure is also included in Fig. 1. The structure is made of pine-wood square rods attached to the corners of a base frame at the bottom and a surface frame at the top. The base frame is fixed to the exciter mount and is made of medium-density fiberboard (MDF) reinforced with an aluminum sheet in order to provide stiffness during oscillation.

A detailed illustration of the surface frame, which has the impingement surface mounted on it, is shown in Fig. 2(a). The base of the surface frame is made of MDF and is attached to the wood rods of the supporting structure. The Inconel-600 foil is sandwiched between two copper bus-bars at each of the two sides parallel to the *Z* axis using nylon and steel fasteners. The steel fasteners acts as points for electrical connections and voltage measurements. The bottom bus-bar on each side is attached to the top side of a wood spacer to provide electrical and thermal insulation between the bus-bars and the aluminum angle sections. Spring loaded steel fasteners are inserted to pass through the wood spacers and aluminum angle sections in order to maintain the foil taut along the *Y* direction. The free sides of the foil, parallel to the *Y* axis and not attached to the bus-bars, rests on wood spacers to avoid foil edge flutter during oscillation. This structure was developed over a period of time, after repeated trial-and-error efforts to achieve the desired impingement surface, without any flutter.

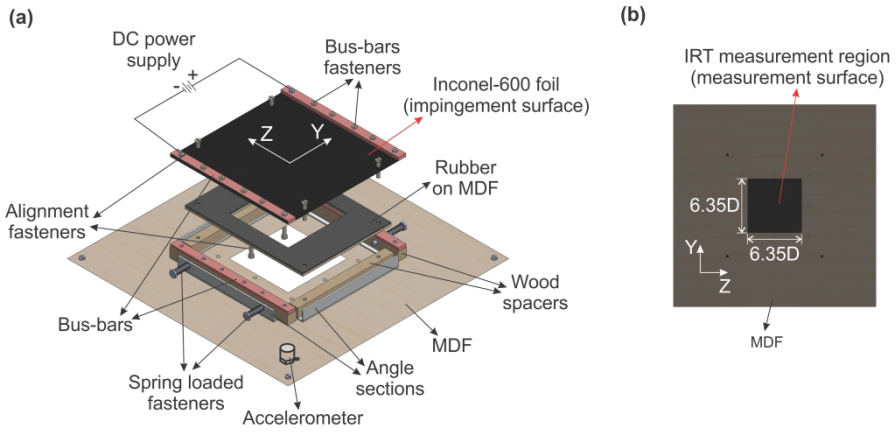

Fig. 2 Impingement surface design: (a) Exploded view of the surface frame; (b) Rear view of the surface frame

During testing of the heated oscillating impingement-surface it was observed that the central area of the foil fluttered even at low oscillation parameter values. Thus to delay this flutter to higher parameter values, a rubber sheet affixed on a MDF sheet is inserted between

the underside of the foil and top side of the wood spacers parallel to the Y axis as shown in Fig. 2(a). In order to finely control the tension in the foil along both Y and Z directions as well as to reduce foil sag in the central area, alignment fasteners are fixed on the top and bottom. These fasteners keep the foil taut by pushing it towards the jet-nozzle exit, which makes the foil surface level rise higher than that of the bus-bars but flush with that of bus-bars fasteners protruding outwards. Pine wood and MDF has been used in the construction of the supporting structure and its parts to decrease the exciter payload to the lowest extent possible. Moreover, all fasteners, except the spring loaded and those meant for electrical connections, are made of nylon to reduce payload weight while also providing electrical and thermal insulation.

As a result of the above mentioned modifications to the impingement surface arrangement the measurement region of the foil on the surface opposite to jet impingement is restricted to an area of $A_{\mathrm{fm}} = 6.35D \times 6.35D$ mm^2, as shown in Fig. 2(b), which shows the view of the surface frame that faces the infrared camera. Both surfaces of the foil are painted with a black heat-resistant paint in order to reduce reflections of the laser light from the impingement surface, and to provide a constant high emissivity and diffused reflective surface for radiation detection on the measurement surface. The foil is electrically heated using direct-current (DC) supplied to the steel fasteners within the bus-bars as shown in Fig. 2(a). These also serve as terminals to measure the potential difference across the foil using a digital multi-meter. The current passing through the foil is measured using a clamp-meter placed around the wire that carries DC current from the power supply unit to the bus-bar terminal. The temperature of the jet at the nozzle-exit is measured using a T-type thermocouple and the ambient room temperature is measured using a digital thermometer.

The electrodynamic exciter and the infrared camera shown in Fig. 1 are placed on separate custom made scissor-jack platforms to allow alignment of centers of the impingement surface and the infrared sensor with the jet axis. The base of the exciter is fixed on a frame with wheels, while the entire jet pipe along with the Y-hydraulic fitting is fixed on movable frame, allowing the positioning of either the impingement surface or the jet-nozzle at a desired mean standoff distance from each other. For PIV experiments the mean standoff distance is set by moving the impingement surface, whereas for IRT experiments it is set by moving the jet pipe. The exciter is powered by a power amplifier and the sinusoidal input signal to the exciter is provided via a function generator. The frequency of surface oscillation f_{s} and its displacement amplitude a_{s} are measured using a single-axis accelerometer mounted on the surface frame as shown in Fig. 2(a). The accelerometer is connected to a double-integrating signal conditioner and its output

is read on a digital oscilloscope, wherein the desired frequencies and displacement amplitude of surface oscillation are achieved by controlling the corresponding settings of the function generator.

2.2 Experimental parameters

The experimental parameters for the system are given in Table. 1. The exact mean standoff distances are H_m/D = 2.03 and 5.09, however for the purpose of discussion in the paper they are referred to with their nominal values as H_m/D = 2 and 5 respectively. These mean standoff distances are the positions where the static surface is placed, and are chosen such that the surface is positioned within the jet potential-core (H_m/D = 2) and in the jet decaying region (H_m/D = 5). The surface is subjected to forced sinusoidal oscillation about the mean standoff distances at a peak-to-peak displacement amplitude a_s, which is approximately equal to 0.2D, and at the frequencies f_s given in Table 1. The peak-to-peak displacement amplitude and frequency of surface oscillation are restricted to a maximum of 2.5 mm and 50 Hz due to the occurrence of foil flutter at values beyond these.

The surface Strouhal number, defined as $St_s = f_s a_s / U_0$, characterizes the oscillatory motion of the surface in the impinging-jet flow, and its values for the two surface oscillation frequencies at the two jet Reynolds numbers are given in Table 1. The values of the velocity ratio, which quantifies the peak velocity v_s attained by the surface during oscillation with respect to the jet bulk-flow speed U_0, are also presented in Table 1. It is observed that the surface reaches a maximum peak velocity of 6.5% of U_0 while oscillating at 50 Hz when the jet impinges with a value of Re = 5000.

Table 1. Experimental parameters for jet impingement on an oscillating surface

D (mm)	H_m/D	Re	U_0 (m/s)	a_s (mm)	f_s (Hz)	St_s	v_s/U_0
12.6	2, 5	5000	6	2.5	20	0.0083	0.0261
					50	0.0208	0.0655
		10000	12		20	0.0041	0.0130
					50	0.0104	0.0327

The instantaneous velocity components in jet impingement on an oscillating surface are measured at 6 phases of the surface motion for an oscillation cycle, as shown in Fig. 3(a) with the corresponding phase angles. As illustrated in Fig. 3(b), three of these phases (ϕ_1, ϕ_2, ϕ_3) occur when the surface moves away from the jet-nozzle exit, while the other three (ϕ_4, ϕ_5, ϕ_6) occur when the surface moves towards the jet-nozzle exit. The position of the static surface,

shown by the red-coloured broken line in Fig. 3(b), coincides with those of phases ϕ_2 and ϕ_5. The physical distance between two consecutive phases, for either surface motions, is approximately 0.8 mm.

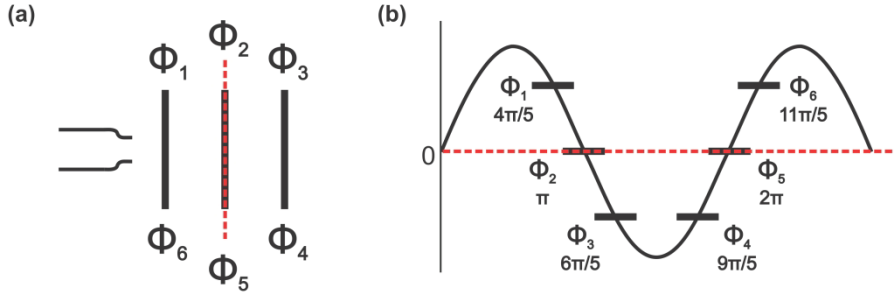

Fig. 3 Impingement surface oscillation: (a) Examined displacement positions of the oscillating surface with respect to the jet-nozzle exit; (b) Phase angles of the displacement positions of the oscillating surface. Broken red coloured lines indicate position of the static impingement surface.

2.3 Particle image velocimetry

The PIV experiments are performed with the jet seeded with atomized olive oil particles having a nominal diameter of 1 μm, which is considered ideal for PIV measurements in air (Raffel et al. 2013). These particles are illuminated by a dual-cavity pulsed Nd:YLF laser (LITRON) at energies of 10 mJ per pulse and a wavelength of 527 nm. The output laser beam is passed through an articulated mirror arm and shaped into a light sheet using a variable-focus light sheet module. The light sheet is approximately 1 mm thick and is aligned vertically along the jet axis as shown in Fig. 1. Single-exposed double-frame images are recorded using a high-speed CMOS camera (Phantom Miro M-310, 1200 × 800 px^2) fitted with a 200 mm AF Micro-Nikkor lens at an aperture of f/5.6. The image magnification is 0.32 resulting in a spatial resolution of 62.7 ± 0.1 μm/px and a depth-of-field of 1.13 mm. The magnification is set such that the desired spatial resolution is same for measurement regions covering the two mean standoff distances between the jet-nozzle exit and the impingement surface.

Since the circular-jet impingement flow is axisymmetric, PIV measurements are acquired in the top-half region above the jet axis as shown in Fig. 1. These measurement regions cover the extent of the standoff distances and also a radius of 3D from the jet axis. The PIV image frame has its X and Y axes parallel and perpendicular to the jet axis respectively as shown in Fig. 1. During surface oscillation, the X dimension of the measurement region changes as the standoff distance varies by 0.2D between the peak positions of the surface. The field-of-view of the camera is set in such a way that it always covers the region between the jet-nozzle exit

and the extrema of the surface at both the mean standoff distances. The light-sheet is focussed such that its thickness is approximately constant between the jet-nozzle exit and the farthest position of the impingement surface from the jet-nozzle exit, for both static as well as oscillating surface conditions.

The PIV recording parameters are given in Table 2. The integral time-scales, given by $t_l = D/U_0$, are 2.1 ms and 1.05 ms for jet Re = 5000 and 10000 respectively. For computation of velocity statistics in jet impingement on a static surface at the two Re values, the recording time between the double-frame images is set approximately 10 times that of the corresponding integral time scales. The recording time between the double-frame images for jet impingement on an oscillating surface at the two Re and the two f_s values are 0.1 times that of the corresponding oscillation time periods, in other words the image acquisition frequency is 10 times that of the corresponding surface oscillation frequency. This is done in order to measure transient flow velocities at various phases of the surface in an oscillation cycle. However, the times between the double-frame images used to compute the phase-average velocity statistics at each of the 6 phases shown in Fig. 3(a) are 50 ms for f_s = 20 Hz and 20 ms for f_s = 50 Hz, which are greater than the integral times scales for the two jet Re values. The position of the oscillating surface is frozen between the two frames of a double-frame image because the pulse delays are of the order 10^{-3} times the time period of surface oscillation. One set of 1000 double-frame images is acquired for jet impingement on a static surface, whereas 10 sets of 1000 double-frame images are acquired for jet impingement on an oscillating surface with each set having 100 surface-oscillation time periods.

Table 2. PIV recording parameters for jet impingement on static and oscillating surfaces

Re	**f_s (Hz)**	**Pulse delay (μs)**	**Time between recorded double-frame images (ms)**
5000	0 (Static)	40	20
	20		5
	50		2
10000	0 (Static)	20	10
	20		5
	50		2

As the position of the surface changes in each double-frame image, an image-processing algorithm has been developed to identify and extract double-frame images that correspond to a given surface-oscillation phase. This algorithm involves four steps and is applied to the first frame of each double-frame image in the ensemble. The first step is to locate

the position of the surface in the pixel space of the entire frame, the second is to distinguish whether this surface displacement position occurred during surface motion away from the jet exit or towards it, the third step verifies whether the position of the surface matches that of a given phase, and the final step is to identify the ensemble image number of the double-frame image that corresponds to a given phase. Upon identifying the image number, the corresponding double-frame images for each phase are extracted for PIV image pre-processing and cross-correlation analysis. The image pre-processing, performed before cross-correlation analysis, involves masking the raw PIV images to crop unwanted regions upstream of the jet-nozzle exit and behind the surface, including the thin illuminated region along the surface. The pixels in these unwanted regions are replaced with an intensity value of 0.

The velocity vectors are calculated over the region of interest with an interrogation area of 16×16 px^2 having a 50% overlap and resulting in a 0.5 mm spacing between the vectors. The PIV analysis is performed using a software application which employs an iterative and adaptive digital PIV cross-correlation algorithm with a multi-pass multi-grid approach including deforming windows and sub-pixel refinement modules (Willert and Gharib 1991; Soria 1996; Scarano 2001). The initial interrogation area is 64×64 px^2 with 2 passes per interrogation domain and a 2-step grid refinement. A No-DC band-pass filter is used to remove background noise from the images. The raw velocity vectors are validated based on a minimum peak ratio of 1.2 (between the 1st and 2nd displacement peak in the interrogation area) and a minimum peak width of 2.5 px, along with a local median validation in a neighborhood of 5×5 px^2. The resulting velocity vector maps are then scanned for any outliers (Westerweel and Scarano 2005) based on a detection threshold of 1.5 and the rejected vectors (if any) are substituted by a median vector. The vectors closest to the surface are obtained from interrogation areas that have their centres located at the surface.

2.3.1 Triple decomposition

The PIV velocity flow-field in jet impingement on an oscillating surface is decomposed using triple decomposition introduced by Hussain and Reynolds (1970), and adopted later by Soria (2015), for analyzing unsteady turbulent flows. The instantaneous velocity vector is decomposed as

$$u_i(\boldsymbol{x},t) = U_i(\boldsymbol{x}) + \tilde{u}_i(\boldsymbol{x},t) + u_i'(\boldsymbol{x},t)\ , \qquad (1)$$

where U_i is the mean velocity, $\tilde{u}_i$ is the phase-correlated velocity, and $u_i^{'}$ is the turbulence velocity fluctuation. In the present flow configuration, $u_1 = u$ is the axial velocity component, $u_2 = v$ is the radial velocity component, and $\boldsymbol{x} = (X, Y)$ are the spatial coordinates.

The mean velocity is defined as

$$U_i(\boldsymbol{x}) = \lim_{\overleftrightarrow{T}\to\infty} \frac{1}{\overleftrightarrow{T}} \int_0^{\overleftrightarrow{T}} u_i(\boldsymbol{x},t)dt \,, \tag{2}$$

with $\overleftrightarrow{T}$ being the total time of velocity sampling, in this case the total number of double-frame images in an ensemble.

The phase-correlated velocity is given by

$$\tilde{u}_i(\boldsymbol{x},t) = \langle u_i(\boldsymbol{x},t)\rangle - U_i(\boldsymbol{x}) \,, \tag{3}$$

wherein $\langle u_i(\boldsymbol{x},t)\rangle$ is the phase-average velocity given by

$$\langle u_i(\boldsymbol{x},t)\rangle = \lim_{N\to\infty} \frac{1}{N} \sum_{n=0}^{N-1} u_i\left(\boldsymbol{x}, t + n\overleftrightarrow{T}_s\right) \,, \tag{4}$$

where N is the number of oscillation cycles and $\overleftrightarrow{T}_s$ is the period of oscillation, which in this case is the time period of surface oscillation. The phase-average velocity represents the average velocity corresponding to a given phase ϕ in the surface oscillation cycle. For jet impingement on a static surface $\tilde{u}_i(\boldsymbol{x},t) = 0$.

The turbulence velocity fluctuation is given by

$$u_i^{'}(\boldsymbol{x},t) = u_i(\boldsymbol{x},t) - \langle u_i(\boldsymbol{x},t)\rangle \,, \tag{5}$$

which for jet impingement on a static surface is equal to $u_i(\boldsymbol{x},t) - U_i(\boldsymbol{x})$. The phase-average velocities at each of the 6 phases of surface oscillation are obtained by averaging over $N = 1000$ oscillation cycles. The mean velocities for jet impingement on a static surface represent the ensemble-average over 1000 double-frame images whereas those for jet impingement on an oscillating surface represent the ensemble-average over the 6 phases.

2.4 Infrared thermography

The Inconel-600 alloy foil that formed the impingement target is electrically heated to provide a constant heat-flux boundary condition. The foil is considered to be thermally thin as

the Biot number $Bi = h_{conv} s_f / k_f$ is << 1, where h_{conv} is the forced-convection heat transfer coefficient. Hence the temperature is assumed to be constant across the thickness of the foil and this allows the measurement of foil temperature from the surface opposite to jet impingement, which in this case is the measurement surface as shown in Fig. 2(b). The infrared camera used to measure the surface temperature operates in the medium infrared range (FLIR X6540sc, 640 × 512 px^2, 1.5 to 5.5 μm) and is fitted with a 12 mm lens that has a fixed aperture of $f/2$. The magnification of thermal images at H_m/D = 2 and 5 is same and is equal to 0.07, resulting in a spatial resolution of 4.55 ± 0.1 px/mm based on the geometric calibration of the images with a thermal calibration target.

The "heated thin-foil" technique proposed by Carlomagno and Cardone (2010) is adopted to determine steady-state convection heat transfer coefficient between the surface and the impinging jet. This technique requires two surface temperature measurements, one without input heat flux to the foil and the other with input heat flux to the foil. Both these measurements are taken at steady-state conditions with the jet impinging on the surface. The surface temperature measured without input heat flux is the adiabatic surface temperature T_{as}, which is taken as the reference temperature as it accounts for both the temperature of the jet T_j and of the ambient fluid T_{am}. The surface temperature measured with input heat flux is the temperature of the heated surface T_s under jet impingement. The electrical power supplied yields an input heat flux value of approximately Q_f = 795 W/m^2, causing the average surface temperature to attain a value of about 21 ˚C higher than the ambient temperature.

For jet impingement on static and oscillating surfaces at each combination of H_m/D and Re, the adiabatic surface temperatures are measured first and the heated surface temperatures are measured later. In all these measurements, the impingement surface is allowed to attain steady-state temperatures during both static and oscillating conditions. The time duration of surface oscillation after which steady-state temperature is measured is kept the same for the two frequencies f_s = 20 Hz and 50 Hz. The jet temperature at the nozzle-exit and the ambient temperature are measured at the beginning and end of each surface temperature measurement.

One set of 2000 thermal images each of the adiabatic surface temperature T_{as} and the heated surface temperature T_s are acquired for both jet impingement on a static surface and on an oscillating surface in order to reduce measurement noise in the calculated mean temperatures. The time between images of the static surface is 50 ms, while that of the oscillating surface at f_s = 20 Hz is 20 ms and at f_s = 50 Hz is 8 ms. The mean values of T_{as} and T_s are obtained upon

averaging over 2000 thermal images in each case, in order to calculate the temperature difference $T_s - T_{as}$ which is used to determine the local forced-convection heat transfer coefficient h_{conv}.

The heat transfer analysis is carried out by performing a steady-state energy balance of the heated foil per unit area per unit time and is given by

$$Q_f = Q_{fconv} + Q_{rad} + Q_{nconv} + Q_{cond}\,, \tag{6}$$

where Q_f is the input heat flux to the foil, Q_{fconv} is the forced-convection heat flux, Q_{rad} is the radiation heat flux from the two surfaces of the foil, Q_{nconv} is the natural-convection heat flux from the measurement surface, and Q_{cond} is the conduction heat flux within the foil. The local forced-convection heat transfer coefficient is then defined as

$$h_{conv} = \frac{Q_{fconv}}{T_s - T_{as}} = \frac{Q_f - Q_{rad} - Q_{nconv} - Q_{cond}}{T_s - T_{as}} \tag{7}$$

The input heat flux to the foil is

$$Q_f = \frac{V_f I_f}{A_f}\,, \tag{8}$$

where V_f is the potential difference across the foil, I_f is the current supplied to heat the foil, and A_f is the total heated area of the foil.

The radiation heat flux is given by

$$Q_{rad} = 2\varepsilon\sigma(T_s^4 - T_{am}^4)\,, \tag{9}$$

where ε is emissivity of the measurement surface, σ is the Stefan-Boltzmann constant, and T_{am} is the ambient temperature. The emissivity of the black-paint coated foil is measured using an emissometer and is found to be 0.88.

The natural-convection heat flux is determined from the correlation between Nusselt number *Nu* and Rayleigh number *Ra* for a vertical flat plate provided by Fujii and Imura (1976). The natural-convection heat flux is given by

$$Q_{nconv} = \frac{0.56kRa^{1/4}(T_s - T_{am})}{(A_{fm}/P_{fm})}\,, \tag{10}$$

where $Ra = GrPr$ and $Gr = \dfrac{\left(A_{\mathrm{fm}}/P_{\mathrm{fm}}\right)^3 g\beta(T_s - T_{am})}{\nu^2}$

In Eqn. (10), the Grashof number *Gr* is based on a length scale $A_{\mathrm{fm}}/P_{\mathrm{fm}}$, which is the ratio of the measurement foil area to its perimeter. The Prandtl number *Pr* of air is taken to be 0.71, β is the volumetric thermal expansion coefficient of air, which is taken to be $1/T_{\mathrm{am}}$, ν is the kinematic viscosity of air at ambient temperature, and k is the thermal conductivity of air at ambient temperature.

The conduction heat flux within the foil is given by

$$Q_{\mathrm{cond}} = -\, s_{\mathrm{f}} k_{\mathrm{f}} \nabla^2 T_{\mathrm{s}} \tag{11}$$

The Laplacian operator can be evaluated along the spatial coordinates of the surface as

$$\nabla^2 T_s = \frac{\partial^2 T_s}{\partial Y^2} + \frac{\partial^2 T_s}{\partial Z^2} \tag{12}$$

However, the direct calculation of this Laplacian amplifies the inherent random noise in infrared thermal images which cannot be reduced to an acceptable level only by temporal averaging. Various mathematical techniques have been proposed to reduce noise in infrared images by filtering the temperature maps; a few of those can be found in Tsai and Philpot (1998) and Ahnert and Abel (2007). However, in this study the axial symmetry of the temperature map is utilized to filter the spatial temperature field. This is done by performing an azimuthal average of the heated surface temperature resulting in the distribution of surface temperature only along the radial coordinate *R* and thus reducing the Laplacian of Eqn. (12) to a much simpler form given by

$$\nabla^2 T_s = \frac{\partial^2 T_s}{\partial R^2} + \frac{1}{R}\frac{\partial T_s}{\partial R} \tag{13}$$

These spatial derivatives are then evaluated using central finite-difference formulas but with a step size of 3 pixels in order to further reduce random noise (Astarita and Carlomagno 2012).

The Nusselt number *Nu* is then determined from

$$Nu = \frac{h_{\mathrm{conv}} D}{k} \tag{14}$$

2.5 Uncertainty analysis

The uncertainty in the measurement of peak-to-peak displacement amplitude a_s of surface oscillation is ±6.03% while that of *Re* is ±6.62%. The PIV measurement error in the estimation of a displacement vector is expressed as a sum of the bias and random errors. In addition, there is also a sampling error that arises due to ensemble averaging used for the determination of statistical quantities. The bias error is very small when compared to the PIV random error, and is usually negligible if the particle image diameter is about 2 pixel units, which minimizes the pixel-locking bias error as well (Raffel et al. 2013). In flows having a high turbulence intensity, such as jet flows, the PIV random error is small when compared to the rms velocity fluctuations (Adrian and Westerweel 2011). In the present jet flow, the rms axial velocity fluctuations in the free-jet shear layer for Re = 5000 is $O(10)$ larger than the PIV random error. Therefore, the uncertainties in the data presented here are for the statistical sampling analysis only. The uncertainties in the measurements of the mean velocity components and determination of turbulence statistics are calculated based on methods outlined by Benedict and Gould (1996) and Adrian and Westerweel (2011), whereas uncertainties in the derived quantities are calculated using a root-sum-square method (Moffat 1988) applied to their finite difference formulas. The uncertainty values of the quantities reported in Table 3 are percentage relative uncertainty estimates with a 95% confidence interval.

Table 3. Uncertainty estimates for ensemble-average quantities obtained from PIV measurements

Quantity	**Percentage relative uncertainty**
Mean axial velocity U	0.18
Mean axial velocity V	1.18
RMS axial velocity fluctuation u_{rms}	5.07
RMS radial velocity fluctuation v_{rms}	3.78
Reynolds stress $\overline{u'v'}$	13.27
Mean axial strain rate $\frac{\partial U}{\partial X}$	1.60
Mean radial strain rate $\frac{\partial V}{\partial Y}$	1.64

The relative uncertainties in the heat transfer quantities determined from IRT measurements are calculated based on the methods outlined by Moffat (1988), and are reported in Table 4 with a 95% confidence interval. The uncertainties in the measured heated surface temperature T_s and the adiabatic surface temperature T_{as} are determined at the stagnation point for jet impingement on an oscillating surface at H_m/D = 5, Re = 10000 and f_s = 50 Hz. The maximum radiation heat flux Q_{rad}, Eqn. (9), and the maximum natural convection heat flux Q_{nconv}, Eqn.

(10), are estimated to be 7.83% and 4.31% of the input heat flux Q_f, whereas the maximum conduction loss in the foil Q_{cond} due to tangential temperature variation in the measurement region is 2.96% of the input heat flux Q_f. The maximum forced-convection heat flux Q_{fconv} is 96.36% of the input heat flux Q_f. This proportion is largely unchanged for parameters used in this study. The total uncertainty estimated in the determination of *Nu* is ±6.31%.

Table 4. Uncertainty estimates for quantities obtained from IRT measurements

Quantity	**Percentage relative uncertainty**
Electrical potential difference across the foil V_f	2.61
Current supplied to the foil I_f	2.64
Heated surface temperature T_s	0.41
Adiabatic surface temperature T_{as}	0.44
Ambient temperature T_{am}	0.41
Input heat flux to the foil Q_f	2.45
Radiation heat flux Q_{rad}	4.42
Natural convection heat flux Q_{nconv}	5.22
Convective heat transfer coefficient h_{conv}	6.31
Nusselt number *Nu*	6.31

3. Results

The fluid dynamics results are presented first, beginning with a characterization of the free-jet at the jet-nozzle exit and along the jet-centerline. These are followed by the phase-average and mean velocities, rms turbulence velocity fluctuations, Reynolds stresses, and mean normal and axial strain rates for jet impingement on static and oscillating surfaces. The heat transfer results are presented later, which include the steady-state mean surface temperature and Nusselt number maps and the mean azimuthal-average Nusselt number distribution along the radial coordinate for jet impingement on static and oscillating surfaces. Locations in the X-Y plane are expressed non-dimensionally with respect to the jet-nozzle exit diameter D and their origin is located at the center of the jet-nozzle exit. The mean velocity components and statistical turbulence quantities at a given jet Reynolds number are expressed non-dimensionally based on the corresponding jet bulk-flow speed U_0 (Table 1).

3.1 Free-jet characteristics

The flow characteristics of free-jet (in absence of the impingement surface) at the two jet Reynolds numbers are shown in Fig. 4. The mean velocity U/U_0 and turbulence intensity u_{rms}/U_0 profiles at the jet-nozzle exit ($X/D = 0$) are shown in Fig. 4(a). The velocity variation depicts a rectangular exit profile typical for convergent nozzles. For comparison, the velocity profile from Todde et al. (2009) of an axisymmetric jet arising from a circular convergent nozzle at $Re = 2700$, at an axial location $X/D \approx 0.025$, is shown in Fig. 4(a) by the solid line. The gradual drop in velocity observed at the nozzle edges in the present study is due to the nozzle geometry, in particular, due to the length of the straight section after the contraction. This contributes to a larger boundary-layer displacement thickness of the flow within the nozzle when compared to a short axisymmetric nozzle that generates a perfectly flat rectangular exit velocity profile (Tesar 2008, Todde et al. 2009).

The turbulence intensity distribution is slightly non-uniform at the nozzle edges for $Re = 5000$, but has a nominal value of 30% of the jet bulk-flow speeds at the two jet Reynolds numbers. The decay of jet-centerline mean velocities and the growth of jet-centerline rms velocity fluctuations, normalized by the jet-centerline mean exit velocity U_{cj}, are shown in Fig. 4(b). The potential-core of the jet extends to about $X/D = 3$ for both jet Reynolds numbers, beyond which the jet decays due to mixing with ambient fluid and this increases turbulence intensities at the jet-centerline. For comparison, the mean axial velocity decay on the jet-centerline from Todde et al. (2009) for $Re = 5400$ is shown in Fig. 4(b), which exhibits a lower

potential-core length. The variation of jet-centerline mean velocities with axial distance shown in Fig. 4(b) substantiates the positioning of the impingement surface at the two mean standoff distances, one within the jet potential-core ($H_m/D = 2$) and the other in the jet decaying region ($H_m/D = 5$).

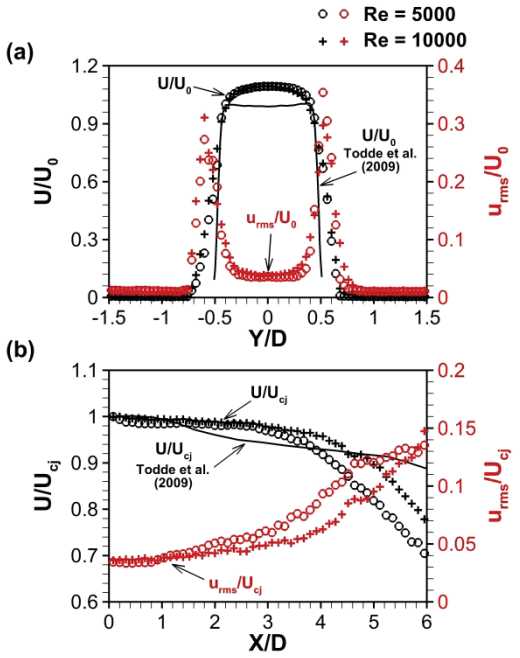

Fig. 4 Free-jet characteristics: (a) Mean axial velocities U/U_0 and rms axial velocity fluctuations u_{rms}/U_0 at the jet-nozzle exit $X/D = 0$. Solid line represents U/U_0 from Todde et al. (2009) at $X/D \approx 0.025$ and $Re = 2700$; (b) Mean axial velocities U/U_{cj} and rms axial velocity fluctuations u_{rms}/U_{cj} along the jet-centerline $Y/D = 0$. Solid line represents jet-centerline U/U_{cj} from Todde et al. (2009) for $Re = 5400$

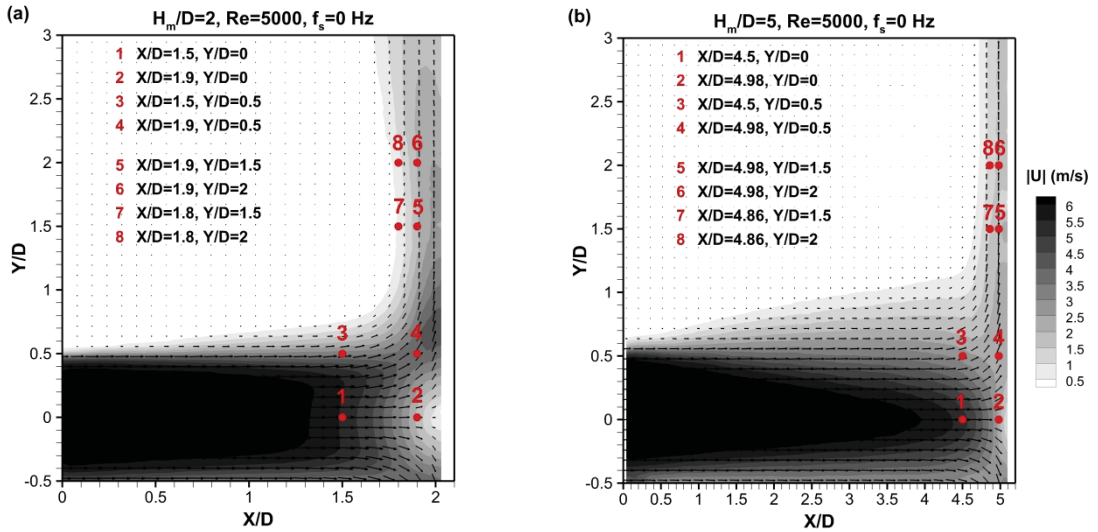

Fig. 5 Spatial locations in the flow field at which phase-average velocities for jet impingement on an oscillating surface are examined. These locations are shown in the mean velocity vector field for jet impingement on a static surface ($f_s = 0$ Hz) for $Re = 5000$ at: (a) $H_m/D = 2$; (b) $H_m/D = 5$. The contours are of the velocity magnitudes $|U|$ (m/s)

3.2 Phase-average velocities

The phase-average velocity components for jet impingement on an oscillating surface are examined at different spatial locations in the impingement and wall-jet regions and their variations with surface-oscillation phases are analysed in comparison with the mean velocity components for jet impingement on a static surface and with the variation of surface velocity during oscillation. The examined spatial locations are indicated in the mean velocity vector field for jet impingement on a static surface at $H_m/D = 2$ and 5, $Re = 5000$ shown in Figs. 5(a) and 5(b) respectively.

The variations of phase-average jet axial velocities $\langle u \rangle/U_0$ with surface-oscillation phases for jet impingement on an oscillating surface at $H_m/D = 2$ and 5 are shown in Figs. 6 and 7 respectively. These variations are presented for the two surface-oscillation frequencies $f_s = 20$ Hz and 50 Hz, and jet Reynolds numbers $Re = 5000$ and 10000 at the examined spatial locations in the flow-field. The mean axial velocities U/U_0 for jet impingement on a static surface at the corresponding locations, denoted by $f_s = 0$ Hz and shown by points marked red in colour, are also presented for comparison. The Strouhal number St_s that corresponds to a given combination of f_s and Re has been mentioned in each sub-figure. A representative variation of the surface velocity with phases, over two oscillation cycles, is shown at the bottom of each sub-figure. The surface-oscillation phases are marked on the horizontal axis within the range of $\pi/2$ to $9\pi/2$ radians.

During the motion of the surface away from the jet-exit, the surface velocity is in the same direction as the axial velocity of the jet, as the surface accelerates from phase ϕ_1 to ϕ_2 and decelerates from ϕ_2 to ϕ_3. In the opposite motion towards the jet-exit, the surface velocity is in the opposite direction to the axial velocity of the jet, as the surface accelerates from phase ϕ_4 to ϕ_5 and decelerates from ϕ_5 to ϕ_6. The variations of phase-average axial velocities for $H_m/D = 2$, $Re = 5000$, $f_s = 20$ Hz ($St_s = 0.0083$) in Fig. 6(a), at locations close to the surface $X/D = 1.9$, $Y/D = 0$ and 0.5 show that phase-average velocities increase from phases ϕ_1 to ϕ_3 and decrease from phases ϕ_4 to ϕ_6, falling behind the variation of surface velocity by $\pi/2$ radians.

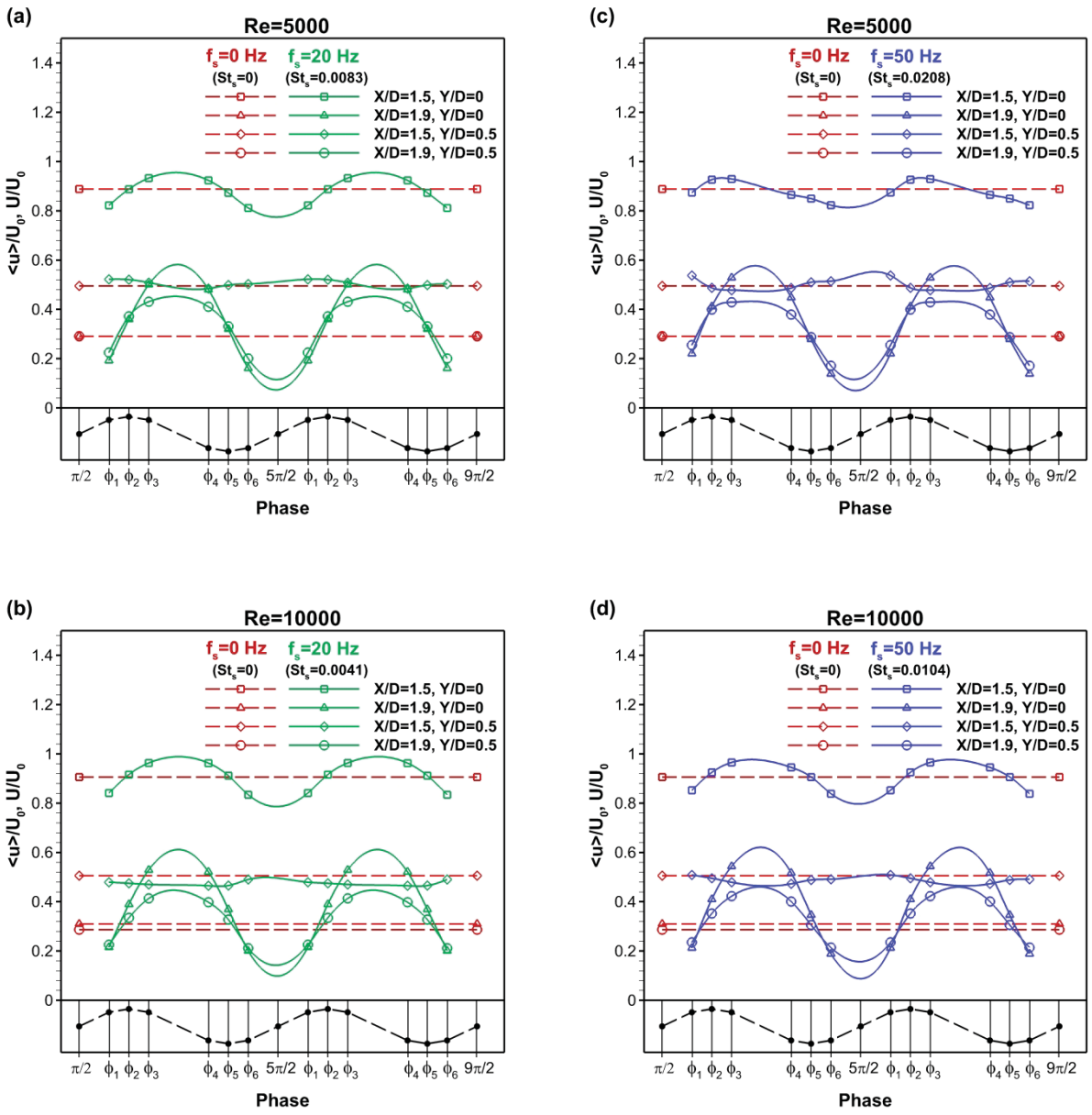

Fig. 6 Variations of phase-average axial velocities $\langle u\rangle/U_0$ with surface-oscillation phases ϕ_1 to ϕ_6 for jet impingement on an oscillating surface at $H_m/D = 2$, at spatial locations $X/D = 1.5$, $Y/D = 0$; $X/D = 1.9$, $Y/D = 0$; $X/D = 1.5$, $Y/D = 0.5$ and $X/D = 1.9$, $Y/D = 0.5$: (a) for $Re = 5000$, $f_s = 20$ Hz ($St_s = 0.0083$); (b) for $Re = 10000$, $f_s = 20$ Hz ($St_s = 0.0041$); (c) for $Re = 5000$, $f_s = 50$ Hz ($St_s = 0.0208$); (d) for $Re = 10000$, $f_s = 50$ Hz ($St_s = 0.0104$). The points marked in red in each of these figures are the mean axial velocities U/U_0 for jet impingement on a static surface $f_s = 0$ Hz ($St_s = 0$) at $H_m/D = 2$, at the corresponding spatial locations. At the bottom of each figure is the representative variation of the surface velocity in two oscillation cycles.

Moving away from the surface towards the jet-nozzle exit, at X/D = 1.5, in Fig. 6(a), the variation of phase-average axial velocities at X/D = 1.5, Y/D = 0 is $\pi/2$ radians behind of the variation of surface velocity, while that at X/D = 1.5, Y/D = 0.5 is $\pi/2$ radians ahead. At a higher value of Re = 10000 but at the same value of f_s = 20 Hz (St_s = 0.0041), in Fig. 6(b), the variations at corresponding spatial locations are found to be similar those shown in Fig. 6(a). When surface-oscillation frequency is increased to f_s = 50 Hz at H_m/D = 2, the phase-average axial velocity variations at X/D = 1.9, Y/D = 0 and 0.5, for Re = 5000 and 10000 (St_s = 0.0208 and 0.0104) in Figs. 6(c) and 6(d) respectively, have similar variations to each other, as well as to those at the same locations for f_s = 20 Hz in Figs. 6(a) and 6(b).

The phase-average axial velocity variations for jet impingement at H_m/D = 5, shown in Fig. 7, are plotted for locations X/D = 4.5 and 4.98 which are at equal axial distances from the surface as the locations X/D = 1.5 and 1.9 respectively are from the surface at H_m/D = 2 (see Fig. 5). These locations also are at the same radial distances from the jet-axis, Y/D = 0 and 0.5. The phase-average axial velocity variations for H_m/D = 5, Re = 5000 and 10000, f_s = 20 Hz (St_s = 0.0083 and 0.0041) in Figs. 7(a) and 7(b), correlate with those shown for H_m/D = 2 in Figs. 6(a) and 6(b) respectively, but have lower amplitudes. A similar inference can be drawn, although not entirely, between the phase-average axial velocity variations for H_m/D = 5, Re = 5000 and 10000, f_s = 50 Hz (St_s = 0.0208 and 0.0104) in Figs. 7(c) and 7(d), and those shown for H_m/D = 2 in Figs. 6(c) and 6(d) respectively.

The variations presented in Figs. 6 and 7 show that at locations closer to the surface the axial velocities are more affected by surface oscillation than those away from the surface, where there is higher effective damping due to greater fluid mass between the surface and that location. At locations closer to the surface the axial velocities are low and hence the impinging jet static pressure plays a larger role by interacting with forces produced due to surface motion. The static pressure is highest at Y/D = 0 and decreases with increasing radial distance from the jet-centerline (Bradshaw and Love 1961). This causes higher amplitudes in the phase-average axial velocity variations at the jet-centerline Y/D = 0 than at Y/D = 0.5. The static pressures closer to the surface at Y/D = 0.5 for jet impingement at H_m/D = 5 are lower than those for jet impingement at H_m/D = 2 (Tu and Wood 1996), thus resulting in lower amplitudes of phase-average axial velocity variations at X/D = 4.98, Y/D = 0.5, as observed from Fig. 7.

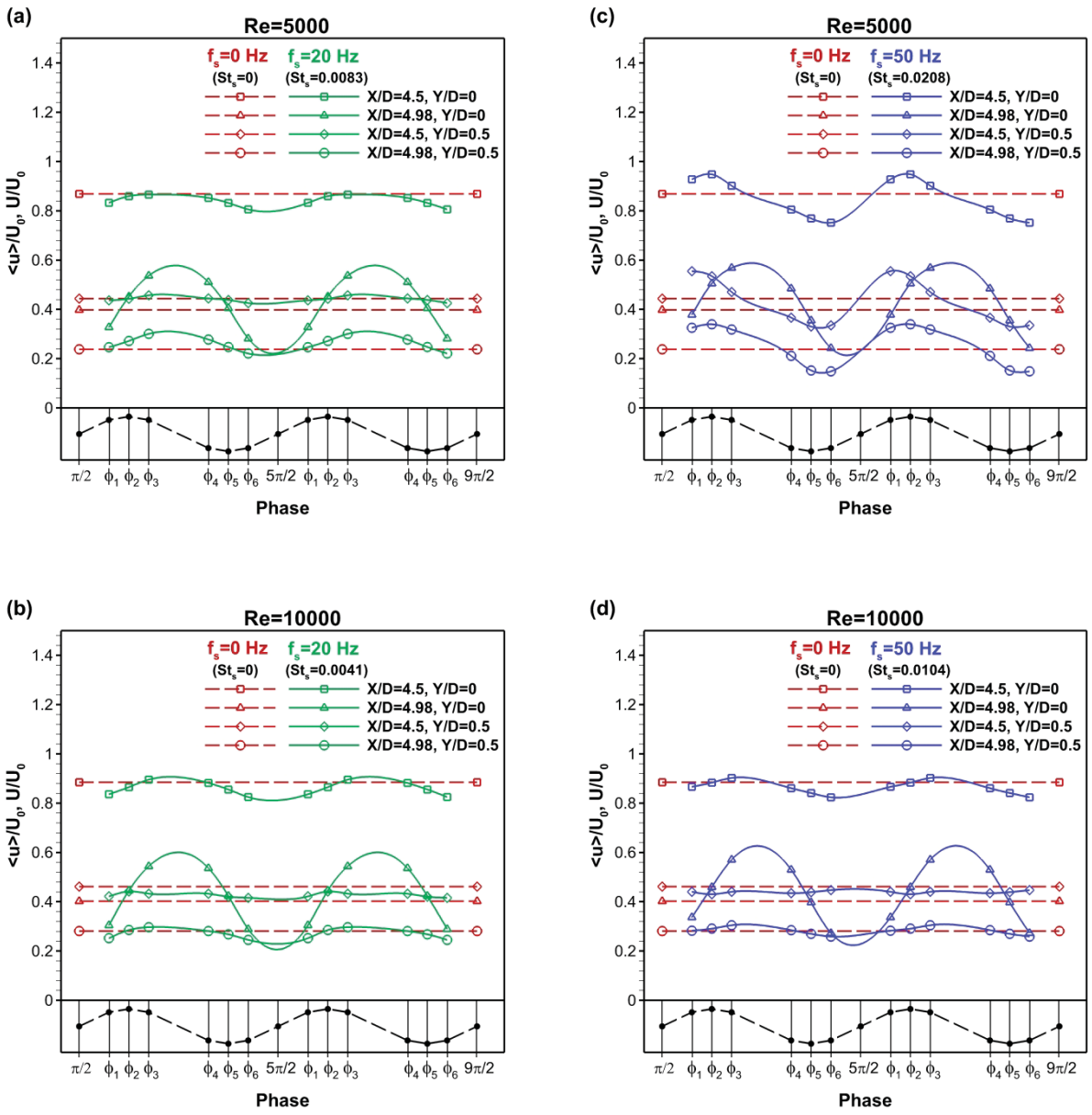

Fig. 7 Variations of phase-average axial velocities $\langle u\rangle/U_0$ with surface-oscillation phases ϕ_1 to ϕ_6 for jet impingement on an oscillating surface at $H_m/D = 5$, at spatial locations $X/D = 4.5$, $Y/D = 0$; $X/D = 4.98$, $Y/D = 0$; $X/D = 4.5$, $Y/D = 0.5$ and $X/D = 4.98$, $Y/D = 0.5$: (a) for $Re = 5000$, $f_s = 20$ Hz ($St_s = 0.0083$); (b) for $Re = 10000$, $f_s = 20$ Hz ($St_s = 0.0041$); (c) for $Re = 5000$, $f_s = 50$ Hz ($St_s = 0.0208$); (d) for $Re = 10000$, $f_s = 50$ Hz ($St_s = 0.0104$). The points marked in red in each of these figures are the mean axial velocities U/U_0 for jet impingement on a static surface $f_s = 0$ Hz ($St_s = 0$) at $H_m/D = 5$, at the corresponding spatial locations. At the bottom of each figure is the representative variation of the surface velocity in two oscillation cycles.

There is no marked difference between the phase-average axial velocity variations shown in Figs. 6(a) and 6(c) for the two values of f_s for jet impingement at $H_m/D = 2$, $Re = 5000$, except for a slightly higher effect of surface oscillation for $Re = 5000$, $f_s = 50$ Hz ($St_s = 0.0208$) at $X/D = 1.5$, $Y/D = 0$ and 0.5 in Fig. 6(c). This results in the phase-average axial velocity variation at $X/D = 1.5$, $Y/D = 0$ to have a phase-lag of $\pi/5$ radians with the variation of surface velocity, when compared to a phase-lag of $\pi/2$ radians at the same location for $Re = 5000$, $f_s = 20$ Hz ($St_s = 0.0083$) in Fig. 6(a). The phase-average axial velocity variations for $H_m/D = 5$, $Re = 5000$, $f_s = 50$ Hz ($St_s = 0.0208$) in Fig. 7(c), also show a higher effect of surface oscillation when compared with those of other parameter combinations for jet impingement at $H_m/D = 5$ in Fig. 7. These observations imply that the level of interaction between an impinging jet and an oscillating surface is greater at larger values of Strouhal number St_s. The variation at $X/D = 4.98$, $Y/D = 0.5$ in Fig. 7(c) is found to be very closely in phase with that of the surface velocity as it occurs at a location closer to the surface where the axial velocity is very low.

The only locations at which the phase-average axial velocity variations are found to be noticeably different, when compared with those at other locations, are $X/D = 1.5$, $Y/D = 0.5$ in Fig. 6 and $X/D = 4.5$, $Y/D = 0.5$ in Fig. 7. These locations are further from the surface and in the free-shear layer where there are low static pressures and high velocity gradients in the radial direction due to jet mixing with the ambient fluid. All these factors contribute to a minimal interaction of the jet with surface oscillation at these locations. However, for $Re = 5000$, $f_s = 50$ Hz ($St_s = 0.0208$), for $H_m/D = 2$ and 5 in Figs. 6(c) and 7(c) respectively, the amplitudes of phase-average axial velocity variations at these locations are higher when compared with other values of St_s.

The variations of phase-average radial velocities $\langle v \rangle/U_0$ with surface-oscillation phases for jet impingement on an oscillating surface at $H_m/D = 2$ and 5, $Re = 5000$ are shown in Fig. 8. These are plotted for spatial locations in the wall-jet indicated in Fig. 5 and they appear along with the mean radial velocities V/U_0 for jet impingement on a static surface at the corresponding locations for comparison. The phase-average radial velocities for both values of f_s are opposite in variation to those of the phase-average axial velocities closer to the surface at $X/D = 1.9$ and 4.98 shown in Figs. 6(a) and 6(c), and 7(a) and 7(c) respectively. These variations occur to satisfy mass conservation during surface oscillation. Furthermore, it is observed that for both values of f_s for jet impingement at $H_m/D = 2$, $Re = 5000$, the phase-average axial velocities at $X/D = 1.9$, in Figs. 6(a) and 6(c), for phases ϕ_1 and ϕ_6 are lower than the mean axial velocity for a static surface, and therefore the phase-average radial velocities at $X/D = 1.9$, in Figs. 8(a)

and 8(b), for these phases are higher than the mean radial velocity for a static surface. The phase-average radial velocities at X/D = 1.8 for phases ϕ_1 and ϕ_6 are also higher the mean radial velocity for a static surface at that location.

The phase-average radial velocity variations for jet impingement at H_m/D = 5 in Figs. 8(c) and 8(d) have lower amplitudes when compared with those for jet impingement at H_m/D = 2 because of similar attributes between the phase-average axial velocity variations at these two mean standoff distances. It is observed that for both values of f_s for jet impingement at H_m/D = 5 the phase-average radial velocities for phases ϕ_1 and ϕ_6 at X/D = 4.98 are lower while those at X/D = 4.86 are higher than the corresponding mean radial velocities for a static surface at those locations. This is in contrast to the findings at H_m/D = 2 where the phase-average radial velocities at both X/D = 1.9 and 1.8 for phases ϕ_1 and ϕ_6 where higher than the corresponding mean radial velocities for a static surface (Figs. 8(a) and 8(b)). The lower phase-average radial velocities for phases ϕ_1 and ϕ_6 at X/D = 4.98 for H_m/D = 5 are due to the effect of wall-shear as these locations lie within the boundary layer when the surface is at phases ϕ_1 and ϕ_6. At all other locations in the wall-jet, X/D = 1.9 and 1.8 for H_m/D = 2 (Fig. 5(a)) and X/D = 4.86 for H_m/D = 5 (Fig. 5(b)), are outside the boundary layer for phases ϕ_1 and ϕ_6 of surface oscillation.

Overall, the amplitudes of phase-average radial velocity variations in Fig. 8 show that radial velocities closer to the surface experience a greater effect of surface-oscillation than those further away from the surface. These variations also show that the phase-average radial velocities are not dependent on the Strouhal number St_s but on the mean standoff distance H_m/D. The phase-average radial velocity variations for Re = 10000 are similar to those for Re = 5000 and so have not been presented.

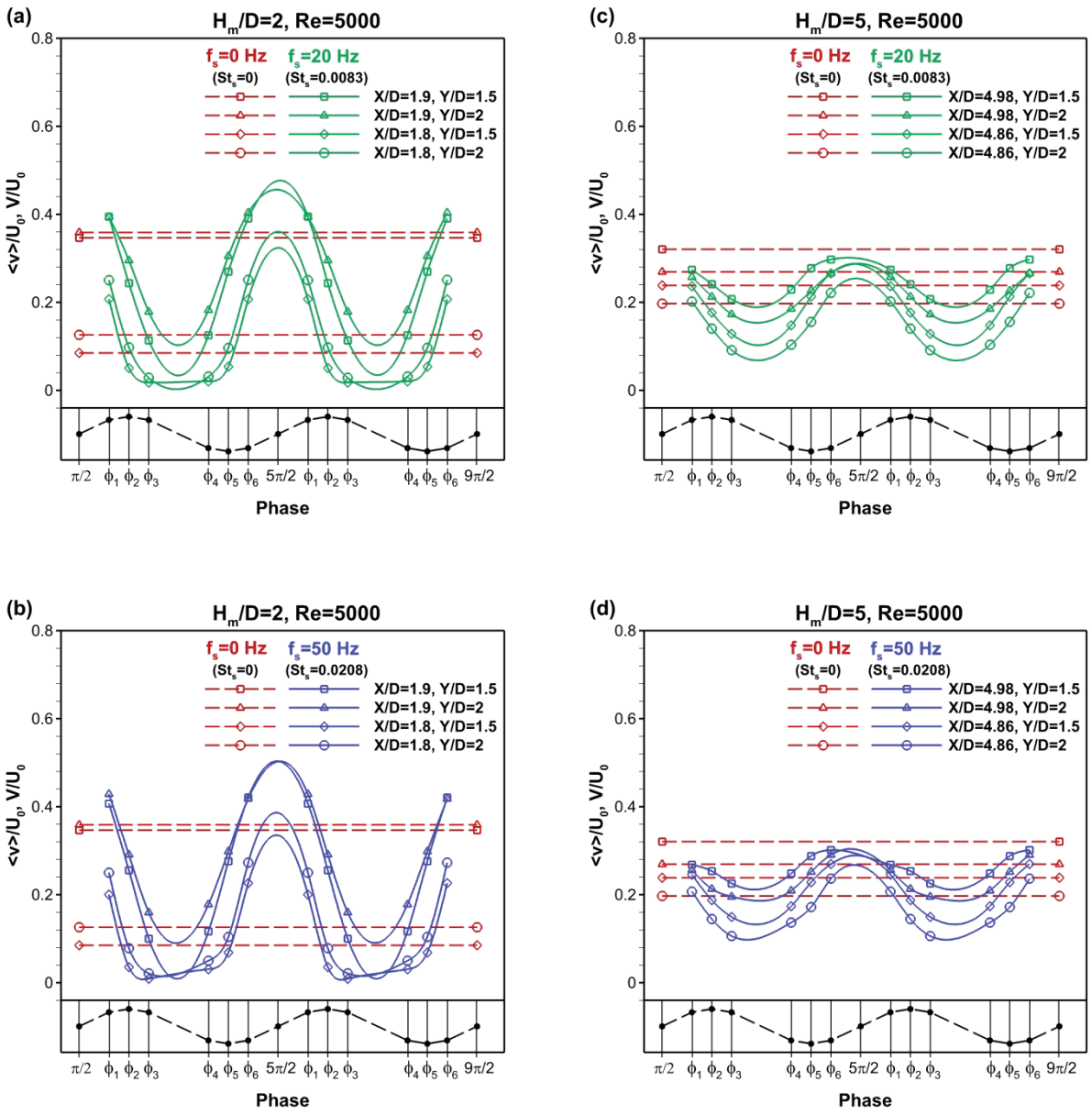

Fig. 8 Variations of phase-average radial velocities $<v>/U_0$ with surface-oscillation phases ϕ_1 to ϕ_6 for jet impingement on an oscillating surface at: $H_m/D = 2$, $Re = 5000$, at spatial locations $X/D = 1.9$, $Y/D = 1.5$; $X/D = 1.9$, $Y/D = 2$; $X/D = 1.8$, $Y/D = 1.5$ and $X/D = 1.8$, $Y/D = 2$; (a) for $f_s = 20$ Hz ($St_s = 0.0083$); (b) for $f_s = 50$ Hz ($St_s = 0.0208$); and at $H_m/D = 5$, $Re = 5000$, at spatial locations $X/D = 4.98$, $Y/D = 1.5$; $X/D = 4.98$, $Y/D = 2$; $X/D = 4.86$, $Y/D = 1.5$ and $X/D = 4.86$, $Y/D = 2$: (c) for $f_s = 20$ Hz ($St_s = 0.0083$); (d) for $f_s = 50$ Hz ($St_s = 0.0208$). The points marked in red are the mean radial velocities V/U_0 for jet impingement on a static surface $f_s = 0$ Hz ($St_s = 0$) at $H_m/D = 2$ in figures (a) and (b), and at $H_m/D = 5$ in figures (c) and (d), at the corresponding spatial locations. At the bottom of each figure is the representative variation of the surface velocity in two oscillation cycles.

3.3 Mean flow characteristics

The mean flow characteristics obtained for jet impingement on an oscillating surface represent mean values over the 6 phases of surface-oscillation investigated, and are compared with corresponding characteristics for jet impingement on a static surface. Figure 9 shows the mean axial velocities U/U_0 for jet impingement on a static and an oscillating surface at H_m/D = 2 and 5, at locations Y/D = 0 and 0.5. The mean axial velocity variation along the axial coordinate at Y/D = 0 for jet impingement on a static surface at H/D = 2, Re = 15895 obtained from Hammad and Milanovic (2011) is presented in Fig. 9(b) for comparison. A fully-developed jet from a long circular pipe was used by Hammad and Milanovic (2011) which explains the departure between these variations for a static surface for X/D < 1.7.

The variation of mean axial velocities along the axial direction are not noticeably different from those for jet impingement on a static surface, except in the impingement region where the mean axial velocities are higher than those for a static surface. These higher mean axial velocities occur at both Y/D = 0 and 0.5 for H_m/D = 2 (Figs. 9(a) and 9(b)), whereas they occur only at Y/D = 0 for H_m/D = 5 (Figs. 9(c) and 9(d)). The increase in mean axial velocities at Y/D = 0.5 for H_m/D = 2 due to surface oscillation indicates a broadening of the jet from that present for a static surface and was also observed by Ichimiya and Yoshida (2009) for a confined slot jet impinging on an oscillating surface. The mean axial velocity for H_m/D = 5, Re = 5000, f_s = 50 Hz just above the surface at Y/D = 0 has a value 30.43% greater than that for a static surface.

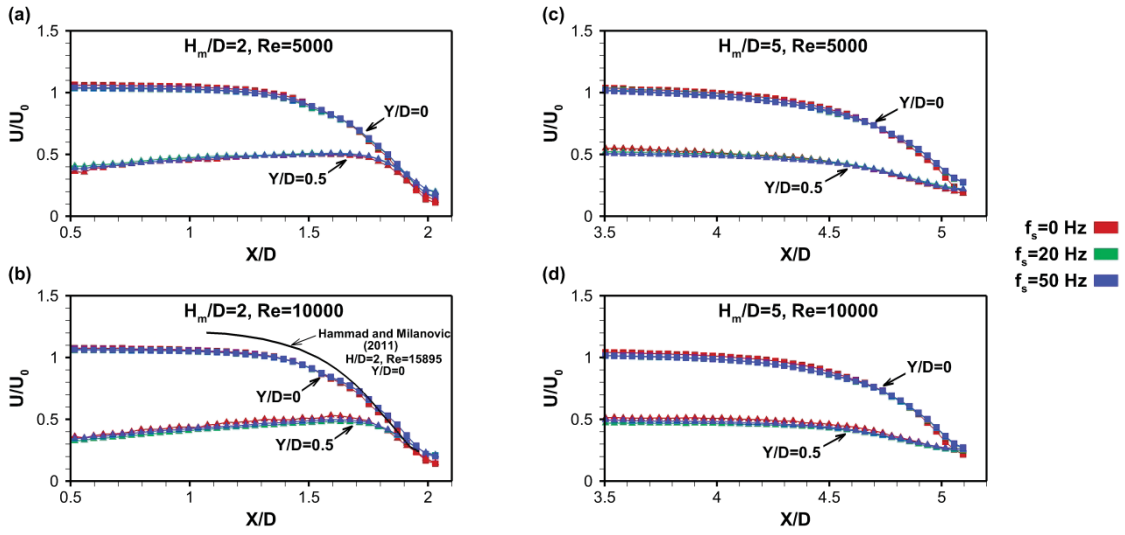

Fig. 9 Mean axial velocities U/U_0 at Y/D = 0 and 0.5 for jet impingement on static and oscillating surfaces for H_m/D = 2: (a) Re = 5000; (b) Re = 10000; and for H_m/D = 5: (c) Re = 5000; (d) Re = 10000. Solid line in (b) represents U/U_0 at Y/D = 0 from Hammad and Milanovic (2011) for jet impingement on a static surface at H/D = 2, Re = 15895.

There is an opposite effect of surface oscillation on the mean radial velocities, as shown in the velocity profiles in Fig. 10, where the mean radial velocities V/U_0 for jet impingement on an oscillating surface are lower than those for a static surface. This occurs not only due to mass conservation but also due to the effect of surface oscillation on large-scale structures in the impingement and wall-jet regions which inhibits their formation and interaction with the surface when compared to that present in the case of a static surface. The largest difference between the mean radial velocities for jet impingement on an oscillating and a static surface at $H_m/D = 2$ occurs at $Y/D = 1$ where the mean radial velocity for $Re = 5000$, $f_s = 50$ Hz is 14.37% lower than that for a static surface, whereas for $H_m/D = 5$ it occurs at $Y/D = 1.5$ where the mean radial velocity for $Re = 5000$, $f_s = 50$ Hz is 20.58% lower than that for a static surface. Overall, the profiles shown in Fig. 10 indicate a decreasing effect of surface oscillation on the mean radial velocities in the wall-jet as the radial distance increases.

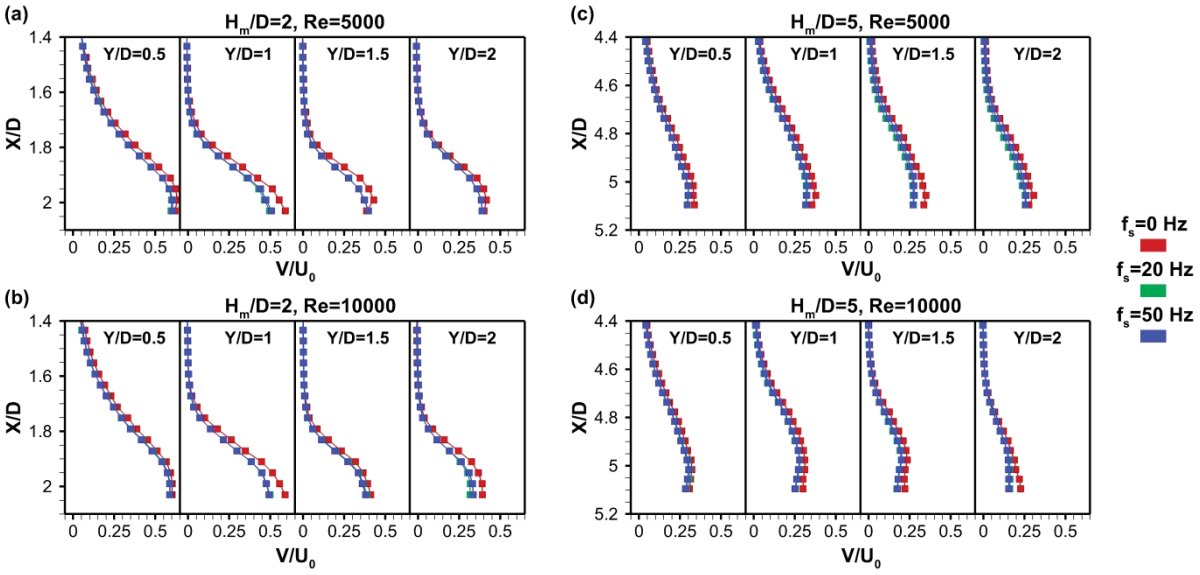

Fig. 10 Mean radial velocities V/U_0 for jet impingement on static and oscillating surfaces at $Y/D = 0.5$, 1, 1.5 and 2 for $H_m/D = 2$: (a) $Re = 5000$; (b) $Re = 10000$; and for $H_m/D = 5$: (c) $Re = 5000$; (d) $Re = 10000$

The rms axial velocity fluctuations u_{rms}/U_0 for $H_m/D = 2$, $Re = 5000$ and 10000 are presented in Figs. 11(a) and 11(b) for locations Y/D = 0.5 and 1.5. These profiles show that surface oscillation lowers turbulence intensities in the free-jet shear layer at Y/D = 0.5 for H_m/D = 2 when compared with a static surface, but increases turbulence intensities at locations closer to the surface. An opposite variation is observed at locations closer to the surface at Y/D = 0.5 for H_m/D = 5 in Figs. 11(c) and 11(d). For Re = 5000, f_s = 50 Hz for both H_m/D = 2 and 5, in Figs. 11(a) and 11(c), the rms axial velocity fluctuations at Y/D = 1.5 are higher than those for a static surface, registering a 22.14% increase at a location just above the surface at H_m/D = 2. This indicates that increase in axial turbulence intensities due to the effect of surface oscillation only occur at locations closer to the surface.

In Fig. 12 the rms radial velocity fluctuation v_{rms}/U_0 profiles at various locations along the wall-jet are presented. They show either lower or same levels of radial turbulence intensities for jet impingement on an oscillating surface when compared with those for jet impingement on a static surface. This means that the effect of surface oscillation reduces shear in the wall-jet region. At Y/D = 0.5 for H_m/D = 2, in Figs. 12(a) and 12(b), surface oscillation is observed to have no effect on the rms radial velocity fluctuations. At Y/D = 1 for H_m/D = 2, Re = 10000 in Fig. 12(b), the rms radial velocity fluctuation for f_s = 50 Hz just above the surface is 15.85% lower than that for a static surface.

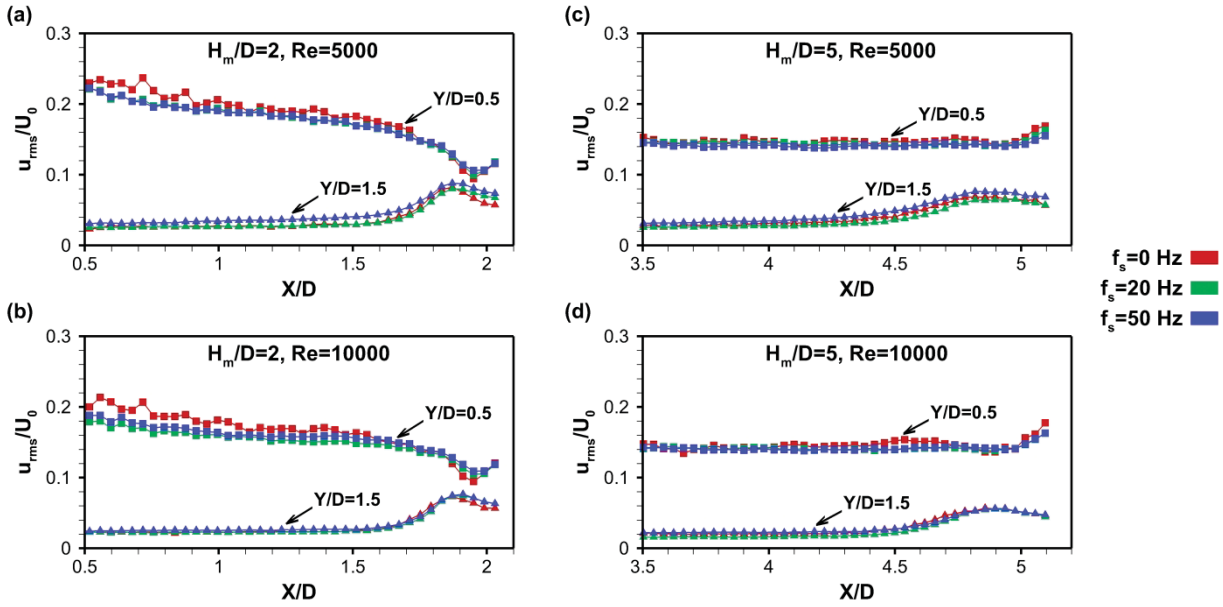

Fig. 11 Root-mean-square axial velocity fluctuations u_{rms}/U_0 for jet impingement on static and oscillating surfaces at Y/D = 0.5 and 1.5 for H_m/D = 2: (a) Re = 5000; (b) Re = 10000; and for H_m/D = 5: (c) Re = 5000; (d) Re = 10000

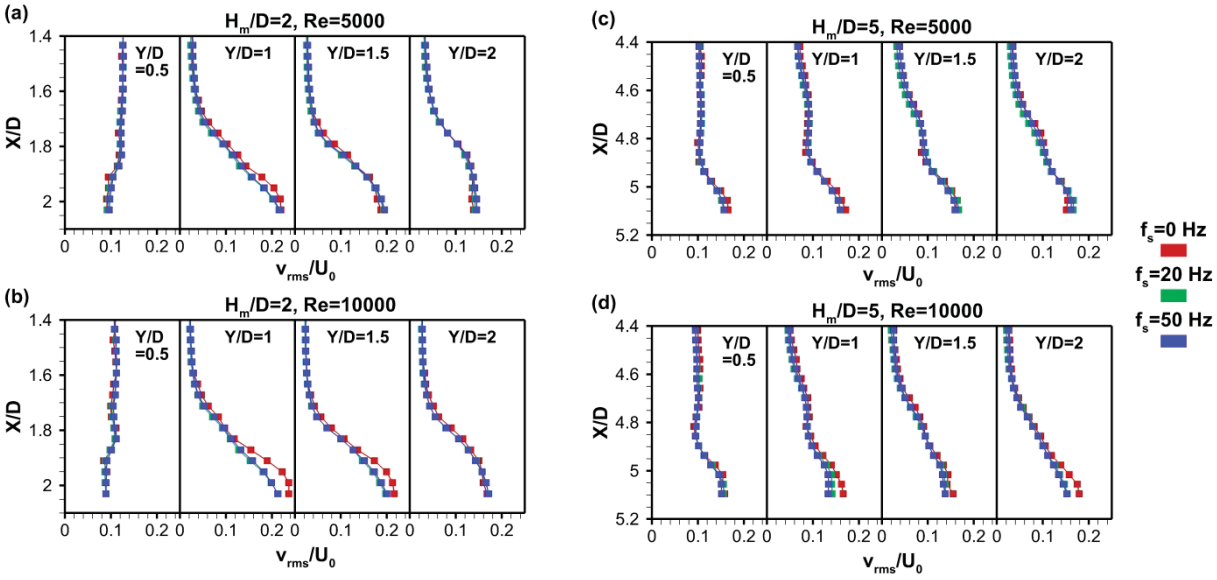

Fig. 12 Root-mean-square radial velocity fluctuations v_{rms}/U_0 for jet impingement on static and oscillating surfaces at Y/D = 0.5, 1, 1.5 and 2 for H_m/D = 2: (a) Re = 5000; (b) Re = 10000; and for H_m/D = 5: (c) Re = 5000; (d) Re = 10000

The Reynolds stress $\langle u'v' \rangle / U_0^2$ variations for jet impingement on static and oscillating surfaces at H_m/D = 2 and 5 are plotted in Fig. 13 at the location Y/D = 0.5. Near the surface for H_m/D = 2, in Figs. 13(a) and 13(b), the Reynolds stress values for an oscillating surface are more negative as compared with those for a static surface, whereas for H_m/D = 5 they are less negative. Surface oscillation has no effect on the Reynolds stress in the free-jet shear layer.The mean axial and radial strain rates, $\partial U/\partial X$ and $\partial V/\partial Y$, at Y/D = 0.5 are shown in Fig. 14. The effect of surface oscillation on these strains rates is found to be greater for H_m/D = 2 than for H_m/D = 5. In the impingement region for H_m/D = 2 in Figs. 14(a) and 14(b), the axial strain rate for an oscillating surface is less negative and the radial strain rate is less positive when compared with that for a static surface. When combined with the mean velocity variations at Y/D = 0.5 in the impingement region (Figs. 9(a) and 9(b) and Figs. 10(a) and 10(b)) it shows that surface oscillation increases axial advection rate and decreases radial advection rate from that present for a static surface. The strain rates for H_m/D = 5 in Figs. 14(c) and 14(d) are almost similar for jet impingement on static and oscillating surfaces, although only a small increase in the axial convection rate is observed for H_m/D = 5, Re = 5000 in the case of surface oscillation.

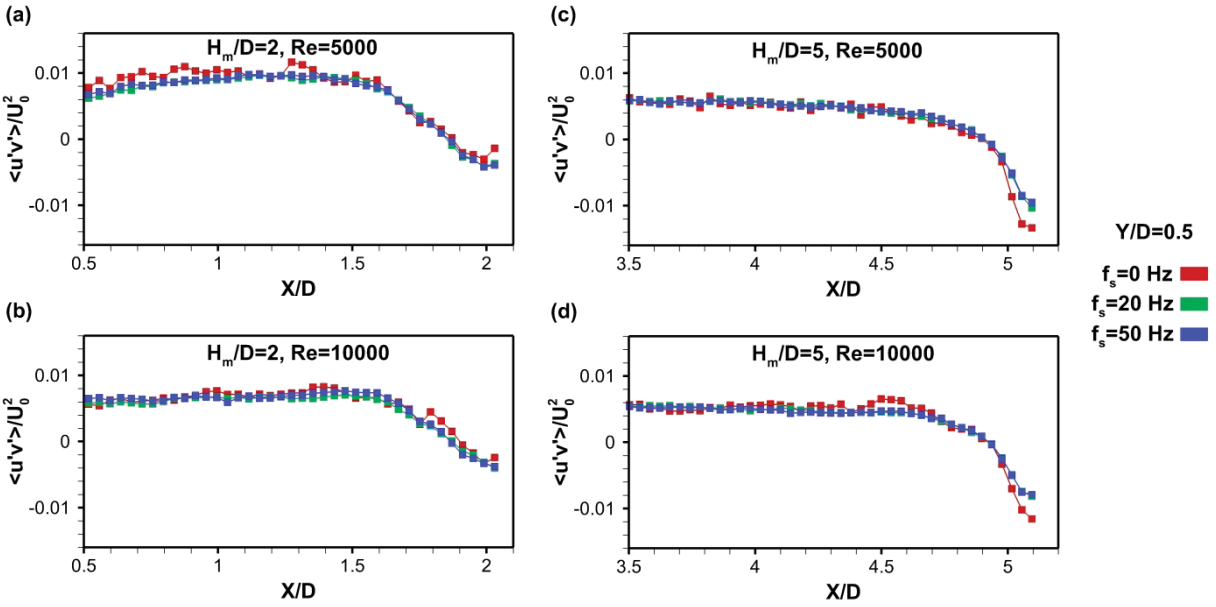

Fig. 13 Reynolds stress $<u'v'>/U_0^2$ for jet impingement on static and oscillating surfaces at $Y/D = 0.5$ for $H_m/D = 2$: (a) $Re = 5000$; (b) $Re = 10000$; and for $H_m/D = 5$: (c) $Re = 5000$; (d) $Re = 10000$

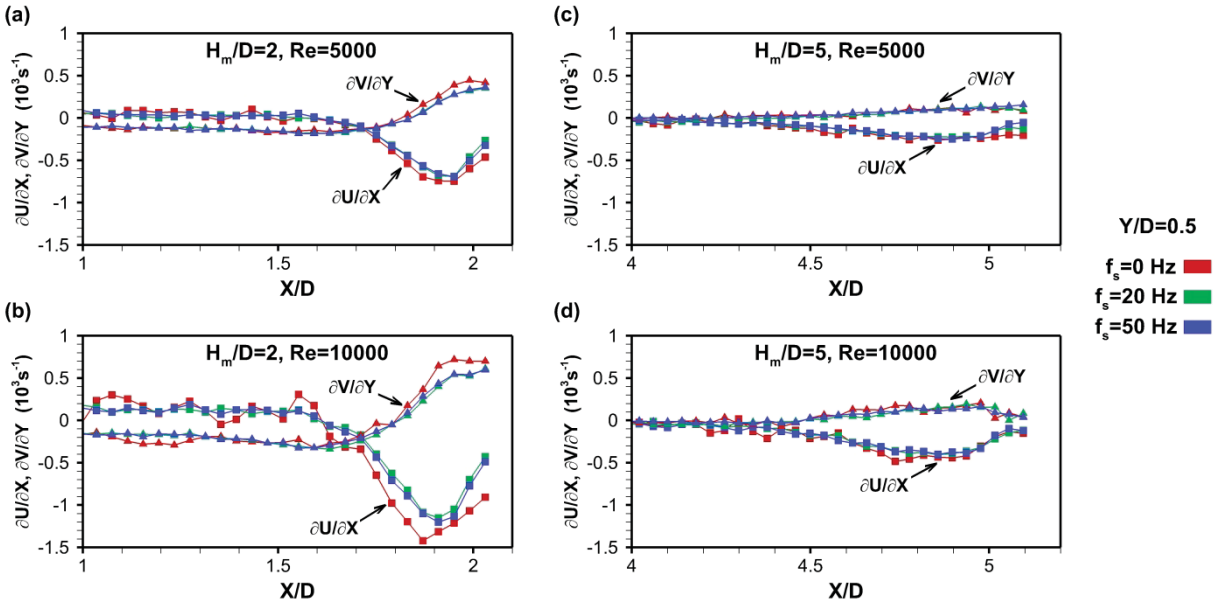

Fig. 14 Mean axial and radial strain rates $\partial U/\partial X$ and $\partial V/\partial Y$ for jet impingement on static and oscillating surfaces at $Y/D = 0.5$ for $H_m/D = 2$: (a) $Re = 5000$; (b) $Re = 10000$; and for $H_m/D = 5$: (c) $Re = 5000$; (d) $Re = 10000$

3.4 Heat transfer results

The mean temperature maps of the steady-state surface temperatures recorded for jet impingement on static and oscillating surfaces at $H_m/D = 2$, $Re = 5000$ are shown in Fig. 15. These mean temperatures are obtained upon averaging over 2000 thermal images. Both adiabatic surface temperature T_{as} and heated surface temperature T_s maps of static and oscillating surfaces are shown. The adiabatic surface temperatures for an oscillating surface are higher than for a static surface and increase with an increase in oscillation frequency, as shown in Figs. 15(a), 15(b) and 15(c). A similar variation is observed in the heated surface temperatures of static and oscillating surfaces as shown in Figs. 15(d), 15(e) and 15(f). The adiabatic and heated surface temperatures for $H_m/D = 2$, $Re = 10000$ and $H_m/D = 5$, $Re = 5000$ and 10000 show similar variations to those presented in Fig. 15 and so have not been shown. A comparison of the mean temperature maps for jet impingement on static and oscillating surfaces shown in Fig. 15 points to a reduction in jet impingement heat transfer rate due to the effect of surface oscillation.

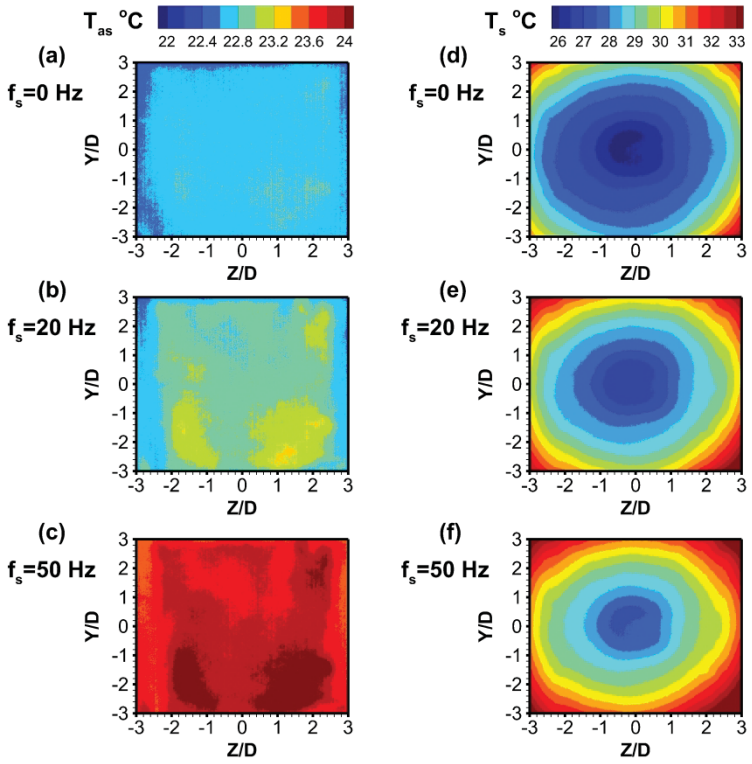

Fig. 15 Steady-state mean thermal maps for jet impingement on static and oscillating surfaces at $H_m/D = 2$, $Re = 5000$. Adiabatic surface temperature T_{as} for: (a) Static surface $f_s = 0$ Hz; (b) Oscillating surface at $f_s = 20$ Hz; (c) Oscillating surface at $f_s = 50$ Hz. Heated surface temperature T_s for: (d) Static surface $f_s = 0$ Hz; (e) Oscillating surface at $f_s = 20$ Hz; (f) Oscillating surface at $f_s = 50$ Hz

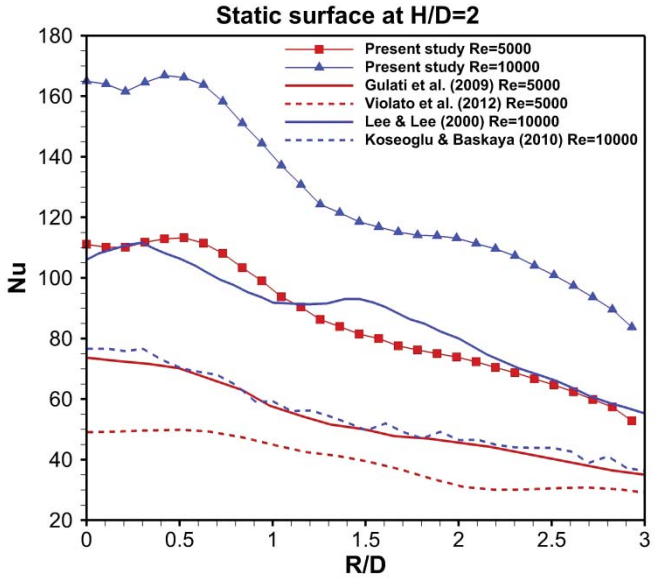

Fig. 16 Comparison of Nusselt number *Nu* variation along the radial coordinate for jet impingement on a static surface at $H/D = 2$ obtained from the present study with previous studies

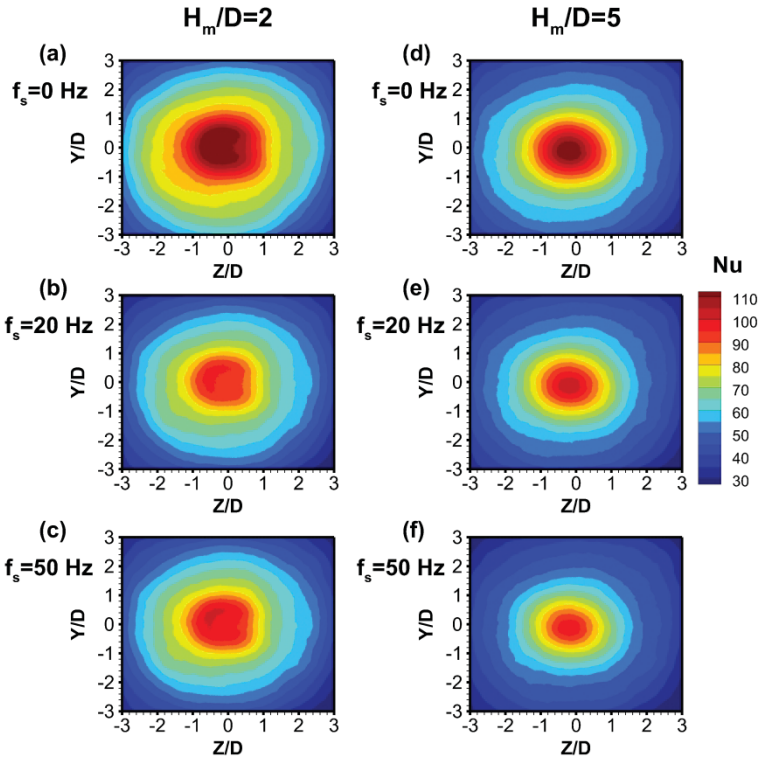

Fig. 17 Nusselt number *Nu* contours for jet impingement on static and oscillating surfaces for $Re = 5000$: (a) Static surface $f_s = 0$ Hz at $H_m/D = 2$; (b) Oscillating surface at $f_s = 20$ Hz at $H_m/D = 2$; (c) Oscillating surface at $f_s = 50$ Hz at $H_m/D = 2$; (d) Static surface $f_s = 0$ Hz at $H_m/D = 5$; (e) Oscillating surface at $f_s = 20$ Hz at $H_m/D = 5$; (f) Oscillating surface at $f_s = 50$ Hz at $H_m/D = 5$.

The heat transfer rate from jet impingement is quantified using the Nusselt number Nu. Before presenting the heat transfer results for jet impingement on an oscillating surface, a comparison of Nu values obtained from the present study for jet impingement on a static surface ($f_s = 0$ Hz) at $H/D = 2$ with previous published studies is presented in Fig. 16. The Nu variations along the radial coordinate R/D are shown for Re = 5000 and 10000. Different nozzle geometries were used in these previous studies: Violato et al. (2012) used a convergent nozzle, Gulati et al. (2009) had a straight circular nozzle, and Lee and Lee (2000) and Koseoglu and Baskaya (2010) used circular orifices. The variations in Fig. 16 show that for a given Re, the Nu values obtained in the present study are higher than those in previous studies at the same value of Re. The four previous studies show considerable disparity between their Nu variations because of different nozzle-exit flow conditions based on their nozzle geometries. These results confirm Herwig (2016): the Nusselt number in a forced-convention heat transfer process depends not only on the forced-convection heat flux at a given fluid temperature (quantity of heat transfer) but also on the temperature difference between the adiabatic and heated surface temperatures at a given fluid temperature (quality of heat transfer). Hence the differences in Nu values observed in Fig. 16 occur due to different nozzle-exit flow conditions, convection heat fluxes, and temperature differences. However, a point of similarity is the secondary Nu peak in the region $1.5 < R/D < 2$ that appears clearly for Re = 10000 in the present study and in that by Lee and Lee (2000) at the same Re.

The Nu contours for jet impingement on static and oscillating surfaces for Re = 5000 at H_m/D = 2 and 5 are presented in Fig. 17. The conduction heat flux loss (Eqn. 11) has been excluded from the computation of these Nu values. The contours of Fig. 17 show that the Nu values for an oscillating surface are lower than those for a static surface but the axi-symmetry observed in the Nu map for a static surface is preserved as well for an oscillating surface. The Nu contours for Re = 10000 at H_m/D = 2 and 5 show similar characteristics to those for Re = 5000 and thus have not been presented.

The azimuthal-average Nusselt numbers Nu_{azm} for jet impingement on static and oscillating surfaces, and their variations along the radial direction R/D for H_m/D = 2 and 5 are shown in Figs. 18(a) and 18(b) respectively. Nu_{azm} represents an average over all local Nu values at a given radius R around the stagnation point $Y/D = 0$. The variations in Fig. 18 show that Nu_{azm} for jet impingement on an oscillating surface at H_m/D = 2 and 5 are lower than those for on a static surface at the corresponding mean standoff distances, and that this reduction in heat transfer rate is greater in the impingement region than in the wall-jet region. At the stagnation

point the *Nu* value for an oscillating surface is lower by 12% to 15% from that for a static surface for the range of parameters considered. The Nu_{azm} values for f_s = 20 Hz and 50 Hz are considered to be similar to each other because the difference between them is lower than the uncertainty in the determination of *Nu*. The results presented in Fig. 18 agree with the findings of Ichimiya and Yoshida (2009) of lower *Nu* values for jet impingement on an oscillating surface when compared with a static surface for all values of f_s considered for H/B = 4 and *Re* = 10000.

It is observed from Fig. 18 that the stagnation point *Nu* for jet impingement on a static surface (f_s = 0 Hz) at H/D = 5 is almost the same as that for H/D = 2, which occurs because the length of the jet potential-core in the present study extends to about X/D = 3 (Fig. 4(b)). When the static surface is positioned at this distance from the jet-nozzle exit, i.e., at H/D = 3, the stagnation point *Nu* attains a maximum value and thereafter decreases with an increase in H/D.

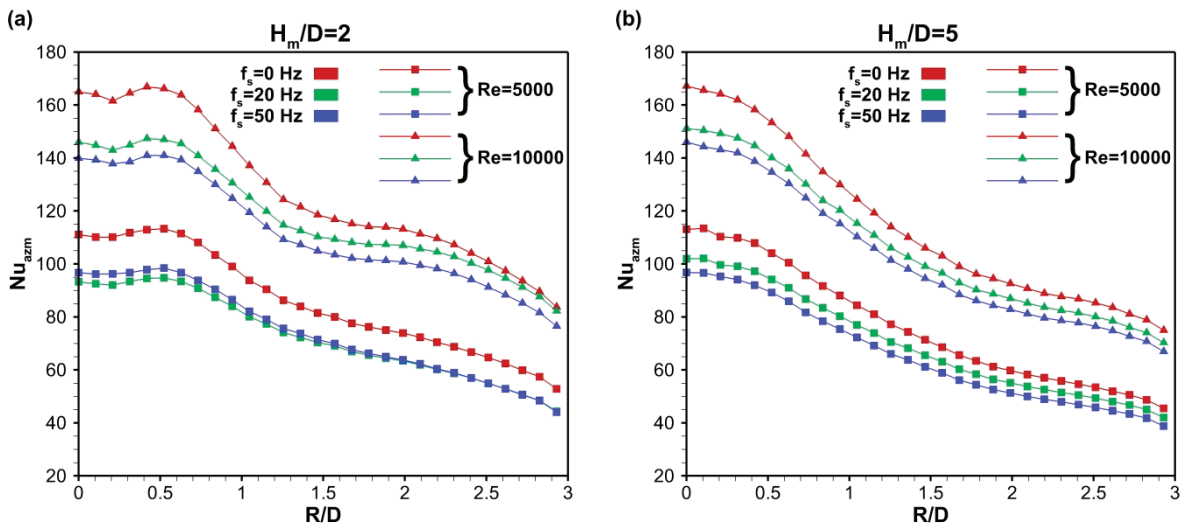

Fig. 18 Azimuthal-average Nusselt numbers Nu_{azm} for jet impingement on static and oscillating surfaces at: (a) H_m/D = 2; (b) H_m/D = 5

4. Discussion

Higher adiabatic surface temperatures for an oscillating surface is primarily because of frictional interaction between the impinging jet and oscillating surface, whereas higher heated surface temperatures for an oscillating surface occur not only due to the aforesaid frictional interaction but also due to the effect of surface oscillation on the impinging jet flow-field. Previous studies on jet impingement on an oscillating surface (Ichimiya and Yoshida 2009; Wen 2005) have not reported on the effect of frictional interaction on surface temperatures.

When the surface is positioned in the jet potential-core region at $H_m/D = 2$ the heat transfer rate mainly depends on the jet velocity, and when it is positioned in the jet decaying region at $H_m/D = 5$ the heat transfer rate depends on both the jet velocity and turbulence intensity. For jet impingement at $H_m/D = 2$, surface oscillation lowers mean axial and radial strain rates in the impingement region when compared with jet impingement on a static surface (Figs. 14(a) and 14(b)), thereby reducing the heat transfer rate. For jet impingement at $H_m/D = 5$, surface oscillation reduces axial and radial turbulence intensities when compared with jet impingement on a static surface (Figs. 11(c), 11(d), 12(c) and 12(d)) and also lowers the mean axial strain rates (Figs. 14(c) and 14(d)), thus lowering the heat transfer rate.

The primary mechanism through which surface oscillation affects the impinging jet-flow is the interaction of surface kinematics with jet axial velocities and large-scale structures. The surface motion is orthogonal to the radial direction and does not directly influence the radial velocities. The variations of radial velocities in the wall-jet are a result of surface oscillation action on the axial velocities (Figs. 6, 7 and 8) and on the large-scale structures in the impingement and wall-jet regions. This results in a greater difference between the mean radial velocities for jet impingement on an oscillating surface and on a static surface when compared to the difference between their mean axial velocities. The effect of surface oscillation is greater in regions of low axial velocities, and is further amplified with an increase in surface oscillation frequency, as observed in Figs. 6(c) and 7(c) and in Figs. 9 and 11 for $Re = 5000$, $f_s = 50$ Hz for both $H_m/D = 2$ and 5.

Surface oscillation strongly interacts with the free-jet at $H_m/D = 2$ but does not do so at $H_m/D = 5$. In both cases the mean radial flow is reduced but the effect is greater at $H_m/D = 2$ (Fig. 10) which means that the formation of wall shear-layer is more greatly impeded at this mean standoff distance. To summarise, an oscillating surface tends to promote vertical motions and inhibits formation of the turbulent wall shear-layer that is principally responsible for heat transfer and its advection out of the system.

The effect of surface oscillation on heat transfer rate is higher in the impingement region $R/D < 1$ than in the wall-jet region because of greater interaction between the jet pressure field, which is higher in the impingement region than in the wall-jet region, and the force generated by surface oscillation. Moving radially farther from the stagnation point, the mean radial velocities and radial turbulence intensities for the static and oscillating surfaces reach values closer to each other (Figs. 10 and 12) and so does the heat transfer rate (Fig. 18). The fluid

dynamics results show that velocities and turbulence intensities at locations in the flow-field closer to the surface are influenced to a greater extent by surface oscillation than those further away from it.

5. Conclusions

An extensive fluid dynamics analysis combined with that of heat transfer for jet impingement on an oscillating surface has been carried out with the results compared with those of jet impingement on a static surface. A non-pulsating jet impinging on an oscillating surface has been studied which complements studies of a pulsating jet on a static surface. The study provides a comprehensive and robust experimental dataset which can be used to validate turbulence models used in computational studies of jet impingement for this class of problems.

Surface oscillation is found to affect the impinging jet flow-field in the near-wall region more than at locations further away from the surface and the intensity of this affect is greater at high surface Strouhal numbers. However, this effect gives rise to lower mean radial velocities, lower turbulence intensities in the free-shear layer and wall-jet region, and lower axial and radial strain rates in the impingement region for jet impingement on an oscillating surface when compared with that on a static surface. Additionally, the impact of an impinging jet on an oscillating surface induces higher surface temperatures due to frictional interaction.

Previous studies on non-pulsating jet impingement on an oscillating surface have mentioned both enhancement and reduction of heat transfer rate from that obtainable from a static surface but the results from the present study clearly show that surface oscillation reduces jet impingement heat transfer rate when compared with that for a static surface, by a maximum value of 15%, for the range of parameters considered in this study. Although the phase-average velocities for jet impingement on an oscillating surface show large amplitude variations about the mean velocities for jet impingement on a static surface, the total effect of surface oscillation on the impinging jet flow-field, over many oscillation cycles, lowers the transport phenomena capabilities of the jet from that present for a static surface.

The surface oscillation frequencies considered in the study are low sub-harmonics of the free-jet vortex generation frequency. It would be interesting to study jet impingement on an oscillating surface at higher frequencies of surface oscillation which can lock-in with the jet vortex generation frequency and might enhance heat transfer. But the practicability of such a system is accompanied by penalties in the form of reduced displacement amplitude of the

surface, high inertial forces acting on the surface, high surface temperatures induced by oscillation, and an expensive cost of implementation.

References

Adrian, R.J. and Westerweel, J., 2011. *Particle image velocimetry* (No. 30). Cambridge University Press.

Ahmed, Z.U., Al-Abdeli, Y.M. and Guzzomi, F.G., 2017. Flow field and thermal behaviour in swirling and non-swirling turbulent impinging jets. *Int J Therm Sci*, 114, pp.241-256.

Ahnert, K. and Abel, M., 2007. Numerical differentiation of experimental data: local versus global methods. *Comput Phys Commun*, 177(10), pp.764-774.

Astarita, T. and Cardone, G., 2008. Convective heat transfer on a rotating disk with a centred impinging round jet. *Int J Heat Mass Trans*, *51*(7-8), pp.1562-1572.

Astarita, T. and Carlomagno, G.M., 2012. *Infrared thermography for thermo-fluid-dynamics*. Springer Science & Business Media.

Benedict, L.H. and Gould, R.D., 1996. Towards better uncertainty estimates for turbulence statistics. *Exp Fluids*, *22*(2), pp.129-136.

Bradshaw, P. and Love, E.M., 1961. *The normal impingement of a circular air jet on a flat surface*. HM Stationery Office.

Carlomagno, G.M. and Cardone, G., 2010. Infrared thermography for convective heat transfer measurements. *Exp Fluids*, *49*(6), pp.1187-1218.

Carlomagno, G.M. and Ianiro, A., 2014. Thermo-fluid-dynamics of submerged jets impinging at short nozzle-to-plate distance: A review. *Exp Therm Fluid Sci*, *58*, pp.15-35.

Chang, S.W., Su, L.M. and Zheng, Y., 2000. Reciprocating impingement jet heat transfer with surface ribs. *Exp Heat Transfer*, *13*(4), pp.275-297.

Choo, K.S. and Kim, S.J., 2010. Comparison of thermal characteristics of confined and unconfined impinging jets. *Int J Heat Mass Trans*, *53*(15-16), pp.3366-3371.

Fujii, T. and Imura, H., 1972. Natural-convection heat transfer from a plate with arbitrary inclination. *Int J Heat Mass Trans*, *15*(4), pp.755-767.

Gardon, R. and Akfirat, J.C., 1965. The role of turbulence in determining the heat-transfer characteristics of impinging jets. *Int J Heat Mass Trans*, *8*(10), pp.1261-1272.

Gauntner, J.W., Hrycak, P. and Livingood, J.N.B., 1970. Survey of literature on flow characteristics of a single turbulent jet impinging on a flat plate. NASA TN D-5652

Gulati, P., Katti, V. and Prabhu, S.V., 2009. Influence of the shape of the nozzle on local heat transfer distribution between smooth flat surface and impinging air jet. *Int J Therm Sci*, 48(3), pp.602-617.

Hammad, K.J. and Milanovic, I., 2011. Flow structure in the near-wall region of a submerged impinging jet. *J Fluid Eng-T ASME*, 133(9), p.091205.

Herwig, H., 2016. What exactly is the Nusselt Number in convective heat transfer problems and are there alternatives?. *Entropy*, 18(5), p.198.

Hrycak, P., 1981. Heat transfer from impinging jets. A literature review. AFWAL-TR-81-3054

Hussain, A.K.M.F. and Reynolds, W.C., 1970. The mechanics of an organized wave in turbulent shear flow. *J Fluid Mech*, *41*(2), pp.241-258.

Ichimiya, K. and Yoshida, Y., 2009. Oscillation effect of impingement surface on two-dimensional impingement heat transfer. *J Heat Transf*, *131*(1), p.011701.

Jambunathan, K., Lai, E., Moss, M.A. and Button, B.L., 1992. A review of heat transfer data for single circular jet impingement. *Int J Heat Fluid Fl*, *13*(2), pp.106-115.

Kanokjaruvijit, K. and Martinez-botas, R.F., 2005. Jet impingement on a dimpled surface with different crossflow schemes. *Int J Heat Mass Trans*, 48(1), pp.161-170.

Klein, D. and Hetsroni, G., 2012. Enhancement of heat transfer coefficients by actuation against an impinging jet. *Int J Heat Mass Trans*, *55*(15-16), pp.4183-4194.

Koseoglu, M.F. and Baskaya, S., 2010. The role of jet inlet geometry in impinging jet heat transfer, modeling and experiments. *Int J Therm Sci*, 49(8), pp.1417-1426.

Lee, J. and Lee, S.J., 2000. The effect of nozzle configuration on stagnation region heat transfer enhancement of axisymmetric jet impingement. *Int J Heat Mass Trans*, 43(18), pp.3497-3509.

Martin, H., 1977. Heat and mass transfer between impinging gas jets and solid surfaces. In *Adv Heat Transf* (Vol. 13, pp. 1-60). Elsevier.

Medina, H., Benard, E. and Early, J.M., 2013. Reynolds number effects on fully developed pulsed jets impinging on flat surfaces. *AIAA J*, *51*(10), pp.2305-2318.

Mobtil, M., Bougeard, D. and Solliec, C., 2014. Inverse determination of convective heat transfer between an impinging jet and a continuously moving flat surface. *Int J Heat Fluid Fl*, *50*, pp.83-94.

Moffat, R.J., 1988. Describing the uncertainties in experimental results. *Exp Therm Fluid Sci*, *1*(1), pp.3-17.

Nasif, G., Barron, R.M. and Balachandar, R., 2015. Simulation of jet impingement heat transfer onto a moving disc. *Int J Heat Mass Trans*, *80*, pp.539-550.

Nasif, G., Barron, R.M. and Balachandar, R., 2015. The application of jet impingement for piston cooling. In the 11th International Conference on Heat Transfer, Fluid Mechanics and Thermodynamics, 20-23 July, South Africa.

Nguyen, T.D., Pellé, J., Harmand, S. and Poncet, S., 2012. PIV measurements of an air jet impinging on an open rotor-stator system. *Exp Fluids*, *53*(2), pp.401-412.

Raffel, M., Willert, C.E., Wereley, S.T. and Kompenhans, J., 2013. *Particle image velocimetry: a practical guide*. Springer.

Scarano, F., 2001. Iterative image deformation methods in PIV. *Meas Sci Technol*, *13*(1), p.R1.

Senter, J. and Solliec, C., 2007. Flow field analysis of a turbulent slot air jet impinging on a moving flat surface. *Int J Heat Fluid Fl*, *28*(4), pp.708-719.

Soria, J., 1996. An investigation of the near wake of a circular cylinder using a video-based digital cross-correlation particle image velocimetry technique. *Exp Therm Fluid Sci*, *12*(2), pp.221-233.

Soria, J., 2015. Experimental studies of the near-field spatio-temporal evolution of zero-net-mass-flux (ZNMF) jets. In *Vortex Rings and Jets* (pp. 61-92). Springer, Singapore.

Tawfek, A.A., 2002. Heat transfer studies of the oblique impingement of round jets upon a curved surface. *Heat Mass Transf*, *38*(6), pp.467-475.

Tesař, V., 2008. Characterisation of subsonic axisymmetric nozzles. *Chem Eng Res Des*, *86*(11), pp.1253-1262.

Todde, V., Spazzini, P.G. and Sandberg, M., 2009. Experimental analysis of low-Reynolds number free jets. *Exp Fluids*, 47(2), pp.279-294.

Tsai, F. and Philpot, W., 1998. Derivative analysis of hyperspectral data. *Remote Sens Environ*, 66(1), pp.41-51.

Tu, C.V. and Wood, D.H., 1996. Wall pressure and shear stress measurements beneath an impinging jet. *Exp Therm Fluid Sci*, *13*(4), pp.364-373.

Violato, D., Ianiro, A., Cardone, G. and Scarano, F., 2012. Three-dimensional vortex dynamics and convective heat transfer in circular and chevron impinging jets. *Int J Heat Fluid Fl*, *37*, pp.22-36.

Viskanta, R., 1993. Heat transfer to impinging isothermal gas and flame jets. *Exp Therm Fluid Sci*, *6*(2), pp.111-134.

Wen, M.Y., 2005. Flow structures and heat transfer of swirling jet impinging on a flat surface with micro-vibrations. *Int J Heat Mass Trans*, *48*(3-4), pp.545-560.

Westerweel, J. and Scarano, F., 2005. Universal outlier detection for PIV data. *Exp Fluids*, *39*(6), pp.1096-1100.

Willert, C.E. and Gharib, M., 1991. Digital particle image velocimetry. *Exp Fluids*, *10*(4), pp.181-193.

Yang, T.L., Chang, S.W., Su, L.M. and Hwang, C.C., 1999. Heat transfer of confined impinging jet onto spherically concave surface with piston cooling application. *JSME Int J B-Fluid T*, *42*(2), pp.238-248.

Zuckerman, N. and Lior, N., 2006. Jet impingement heat transfer: physics, correlations, and numerical modeling. *Adv Heat Transf*, *39*, pp.565-631.